AJS American Journal of Science
publishing earth-sciences research since 1818

Taylor, K., Rauzi, S., Isson, T., Ibarra, D. E., Hülse, D., Kimmig, S. R., Payne, J. L., Altiner, D., Lehrmann, D. J., Kalderon-Asael, B., Planavsky, N. J., & Lau, K. V. (2026). Heterogeneous carbonate lithium isotope records across the end-Permian mass extinction indicate a highly perturbed lithium cycle in the Early Triassic. *American Journal of Science*, *326*, Article 5. https://doi.org/10.2475/001c.156171

Science Paper

Heterogeneous Carbonate Lithium Isotope Records Across the end-Permian Mass Extinction Indicate a Highly Perturbed Lithium Cycle in the Early Triassic

Kaitlin Taylor[1], Sofia Rauzi[2], Terry Isson[2], Daniel E. Ibarra[3], Dominik Hülse[4], Sara R. Kimmig[5], Jonathan L. Payne[6], Demir Altiner[7], Daniel J. Lehrmann[8], Boriana Kalderon-Asael[9], Noah J. Planavsky[9], Kimberly V. Lau[1][a]

[1] Geosciences and Earth and Environmental Systems Institute, Pennsylvania State University, [2] School of Science (Te Aka Mātuatua), University of Waikato, [3] Institute at Brown for Environment and Society and the Department of Earth, Environmental and Planetary Science, Brown University, [4] MARUM, Center for Marine Environmental Sciences, University of Bremen, [5] Institute of Applied Geosciences, Chair of Geochemistry and Economic Geology, Karlsruhe Institute of Technology, [6] Geological Sciences, Stanford University, [7] Geological Engineering, Middle East Technical University, [8] Earth and Environmental Geosciences, Trinity University, [9] Earth and Planetary Sciences, Yale University

Keywords: carbonates, continental weathering, reverse weathering, residence time, lithium isotopes

https://doi.org/10.2475/001c.156171

American Journal of Science

Vol. 326, 2026

Following the end-Permian mass extinction, temperatures remained elevated for ~5 Myr, suggesting a fundamental restructuring of the Earth's climate system. Both a weak silicate weathering feedback and CO_2 release from enhanced marine authigenic clay precipitation are proposed to have sustained elevated temperatures during the Early Triassic. The lithium isotope (δ^7Li) proxy can reveal the roles of terrestrial and marine reverse weathering in maintaining elevated Early Triassic temperatures. We present the first δ^7Li values from Upper Permian to Middle Triassic carbonate strata from the Panthalassa Ocean and the western Tethys Ocean. At the Permian/Triassic boundary, carbonate δ^7Li values in these records, along with previously published data from the eastern Tethys, are consistently below 0‰, and remain low in the Early Triassic. Differences in carbonate δ^7Li values among sections are interpreted as the combined influence of diagenetic alteration and carbonate mineralogy on the isotopic fractionation from co-eval seawater. In the Early Triassic, we observe a large difference between carbonate δ^7Li values and published siliciclastic records following the extinction. Even after accounting for carbonate diagenesis, these paired records imply Li isotope fractionation between carbonate minerals, authigenic marine clay, and seawater that are distinct from modern marine environments. Inferred minimum and maximum constraints on seawater δ^7Li values from these Early Triassic records are also incompatible. We hypothesize that a reduced oceanic Li reservoir—and thus, short residence time—may account for the anomalous Early Triassic δ^7Li records, implying a simultaneous increase in continental weathering and marine clay authigenesis. Heterogeneous seawater δ^7Li records in the Early Triassic could be, therefore, a potential symptom of perturbed carbon-silica cycling that permitted elevated temperatures to persist far longer than the typical timescale for the silicate weathering feedback on Earth's climate.

1. INTRODUCTION

The end-Permian mass extinction (252 Ma) has long been recognized as the greatest biotic catastrophe in the history of complex life (Newell, 1967). Approximately 80% of Changhsingian marine animal genera did not survive into the succeeding Induan stage (Payne & Clapham, 2012), and terrestrial ecosystems were similarly disrupted (e.g., Retallack, 1995). Although the main extinction pulse—tied to Siberian Traps volcanism—occurred in less than 60 kyrs (Burgess et al., 2014), the subsequent recovery of ecosystems was dampened during the next several million years (e.g., Z.-Q. Chen & Benton, 2012; Hallam, 1991). Proxy data have revealed a 10˚C warming of global temperatures that began during the Permian–Triassic (P/Tr) transition and persisted through a 5 Myr interval of delayed or interrupted biotic recovery (Joachimski et al., 2020; Romano et al., 2013; Y. Sun et al., 2012). Although the source and timing of initial P/Tr warming is well established (Burgess et al., 2014), the processes that sustained high CO_2 and allowed for the protracted warm interval remain elusive.

a Corresponding author: kvlau@psu.edu

The Early Triassic was one of the warmest intervals of the past half-billion years on Earth (Isson & Rauzi, 2024; Retallack, 1999). This prolonged warmth extends well beyond the expected timescale of silicate-weathering-driven carbon cycle recovery following a carbon injection event, reflecting a failure of the silicate weathering feedback in regulating climate during this interval (Kump, 2018). High continentality and minimal ongoing tectonic uplift of fresh continental rocks (and therefore the supply of weatherable material) associated with the Pangaean supercontinent have been proposed to have limited continental silicate weathering (Kump, 2018). However, strontium isotope data ($^{87}Sr/^{86}Sr$ ratios) show a rapid rise to higher (i.e., more radiogenic) values during the Early Triassic (Korte et al., 2003; Martin & Macdougall, 1995; Sedlacek et al., 2014; Song et al., 2015; F. Zhang, Romaniello, et al., 2018), which is attributed to an increase in continental weathering during this time. Moreover, the decimation of silica biomineralizers—marked by a "chert gap" observed in Lower Triassic strata (Beauchamp & Baud, 2002; F. Yang et al., 2022)—is proposed to have increased marine dissolved silica concentrations, resulting in enhanced rates of reverse weathering (e.g., marine clay authigenesis) that sustained elevated carbon recycling in the ocean-atmosphere system (Isson et al., 2022; Rauzi et al., 2024). This hypothesis proposes that increased alkalinity consumption via reverse weathering would liberate CO_2 initially captured via silicate weathering, retaining it in the ocean-atmospheric system and maintaining elevated atmospheric pCO_2 (Isson et al., 2020; Isson & Planavsky, 2018). Although definitive evidence for reverse weathering is difficult to obtain from the preserved marine sedimentary record, this positive feedback is hypothesized to have stabilized the Earth's climate system in a greenhouse state during the Early Triassic (Isson et al., 2022; Isson & Planavsky, 2018).

Lithium isotopes ($^{7}Li/^{6}Li$ ratio, reported in delta notation as a $\delta^{7}Li$ value relative to LSVEC, a synthetic lithium carbonate standard) of sediments have emerged as a useful proxy for tracking changes in clay formation in both terrestrial and marine environments (fig. 1; summarized by Pogge von Strandmann, Dellinger, et al., 2021), which can provide insight into continental and reverse weathering during climatic and biospheric perturbations (e.g., Pogge von Strandmann et al., 2013; Pogge von Strandmann, Jones, et al., 2021). The lighter Li isotope (^{6}Li) is preferentially incorporated into clay minerals (Burton & Vigier, 2012; Vigier et al., 2008), which leaves the fluid enriched in the heavier isotope (^{7}Li). In continental settings, riverine $\delta^{7}Li$ values reflect the balance between the dissolution of primary silicate minerals and secondary clay precipitation—or the congruency of weathering (Dellinger et al., 2015; Huh et al., 1998; Misra & Froelich, 2012; Pogge von Strandmann et al., 2013). In addition to continental weathering, about half of the Li input to the ocean is from hydrothermal alteration of ocean crust at mid-ocean ridges, which exhibits a $\delta^{7}Li$ value of ~6‰ (Coogan et al., 2017). The $\delta^{7}Li$ value of hydrothermal fluids does not appear to vary with sediment cover or fluid composition, suggesting it is controlled by deeper processes that are unlikely to change significantly over time (Hathorne & James, 2006). Lithium is removed from seawater via marine clay formation during low-temperature basalt alteration and in the ambient sediment pile (fig. 1). In the modern ocean, these processes are associated with isotope fractionation factors ($\Delta^{7}Li_{fluid\text{-}clay}$) of ~12 to 16‰ and ~20‰, respectively (Chan et al., 2006; Misra & Froelich, 2012; Vigier et al., 2008), but these have likely varied through time due to changes in bottom-water temperature and clay formation rate (Coogan et al., 2017; Kalderon-Asael et al., 2021; F. Li et al., 2021; G. Li & West, 2014). Seawater $\delta^{7}Li$ values reflect the balance of these processes, and therefore, reconstructions of $\delta^{7}Li$ values of seawater can provide insight into Li cycling across climate events (fig. 1).

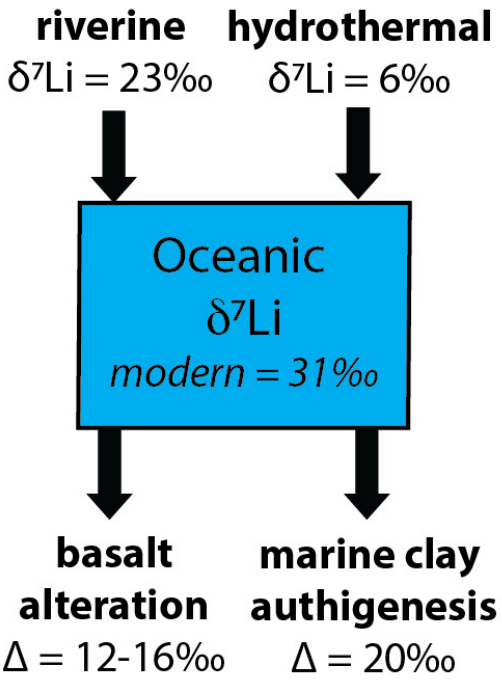

Figure 1. Cartoon of modern $\delta^{7}Li$ mass balance. The $\delta^{7}Li$ value of the dissolved load in rivers to seawater can vary with secondary clay formation and dissolution (e.g., Dellinger et al., 2015). The effective isotope offset between seawater and output fluxes (Δ) also reflects the preferential removal of ^{6}Li into marine clays (G. Li & West, 2014), but can decrease if the rate of marine clay formation and associated Li uptake increases (Kalderon-Asael et al., 2021). For references, see text.

Interpretations of Permian and Triassic $\delta^{7}Li$ records are hampered by a lack of constraints on how this proxy records, or fails to record, the seawater $\delta^{7}Li$ value, as well as the potential for changes in multiple sources or sinks to also drive trends, leading to non-unique explanations for temporal changes in Li cycling (Cao et al., 2022; G. Li & West, 2014; Rauzi et al., 2024; H. Sun et al., 2018). A 600 kyr $\delta^{7}Li$ record from carbonate strata of the main extinction event (H. Sun et al., 2018) does not provide a complete picture of weathering prior to or following the extinction, nor does it follow the carbonate leaching method

widely adopted to isolate Li bound in carbonate minerals while avoiding silicate contamination. A composite Li isotope record from the Middle Permian to the Smithian/Spathian boundary (late Early Triassic) revealed nearly crustal δ^7Li values (i.e., ~0‰; Sauzéat et al., 2015; Teng et al., 2004) in carbonates deposited more than a million years prior to the extinction interval (Cao et al., 2022), with a modest increase to ~5‰ in the Early Triassic. However, this record does not track the recovery into the cooler Middle Triassic. Whether a carbonate record from one location (South China) is representative of the global ocean is also unclear because weathering intensity and diagenetic effects vary spatially. Today, Li is well-mixed in the ocean due to its long residence time relative to ocean circulation (τ = 1.5 Ma; Huh et al., 1998). However, at other times, different ocean basin configurations, ocean circulation patterns, or changes in the global Li budget could result in heterogenous seawater δ^7Li values. Moreover, incorporation of Li during the precipitation of carbonate minerals from seawater can result in variable (*ca.* ~0 to 12‰) isotope fractionation according to the carbonate mineralogy as well as environmental factors such as pH (e.g., Marriott, Henderson, Crompton, et al., 2004; Murphy et al., 2022; Pogge von Strandmann, Schmidt, et al., 2019). Therefore, comparing δ^7Li records from several paleogeographic locations can help to evaluate if a global signal can be reconstructed or whether records are impacted by local factors such as diagenesis, differences in carbonate mineralogy, or heterogeneity of seawater δ^7Li values.

We address these current knowledge gaps with δ^7Li analysis from carbonate successions from two distinct paleogeographic sites that extend the carbonate δ^7Li record to the Middle and Late Triassic. As the first study to compare differences among co-eval carbonate sections, records from the Panthalassa Ocean and the Western Tethys, combined with published records from the Eastern Tethys (Cao et al., 2022), can provide a more detailed picture of the factors influencing carbonate δ^7Li values on the global scale. These records are compared with marine siliciclastic δ^7Li records (Rauzi et al., 2024). Siliciclastic δ^7Li records reflect changes in isotopic composition and relative proportions of terrestrial material and marine authigenic clay, which may provide insight into continental weathering and marine clay authigenesis (i.e., reverse weathering). By interrogating the differences between the δ^7Li records of these sedimentary archives, we propose further constraints on Li cycling during this climatically unique interval.

2. MATERIALS AND METHODS

2.1. Geologic Materials

Carbonates from two stratigraphic sections in Turkey and Japan were analyzed to complement existing carbonate δ^7Li records from South China, thus expanding the spatial coverage to the western Tethys and Panthalassa Oceans and temporal coverage into the Middle and Late Triassic (fig. 2). The Upper Permian to Middle Triassic stratigraphy of the Taşkent (Turkey) section has been published previously (Lau et al., 2016, 2017; Payne et al., 2007). The age model (updated from Lau et al., 2016, 2017) is based on biostratigraphic, lithostratigraphic, and carbon isotope chemostratigraphic correlation to the well-dated Guandao (South China) section (Altıner et al., 2021; Lehrmann et al., 2015). The Takachiho (Japan) section was correlated to Taşkent using carbon isotope chemostratigraphy and lithostratigraphy (figs. 3 and 4), as well as conodont biostratigraphy from Takachiho (L. Zhang et al., 2019). Constant sedimentation rates were assumed and were interpolated from known chemostratigraphic, biostratigraphic, and other known tie points (generally, U-Pb geochronology). Based on these age models, samples from Taşkent are constrained to range in age from 253 Ma in the Changhsingian to ~235 Ma in the Ladinian (Middle Triassic). Samples from Takachiho are constrained to range from 255.8 Ma in the Changhsingian to *ca.* 235.5 Ma in the Carnian.

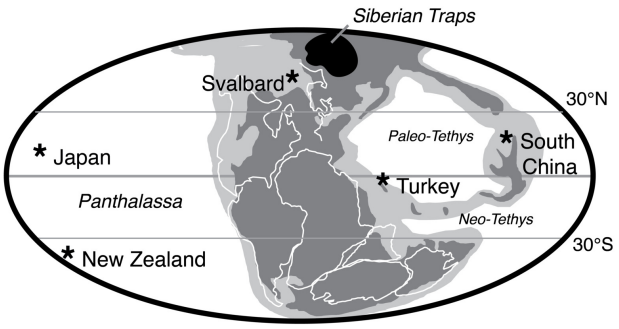

Figure 2. Paleogeographic map of Early Triassic δ^7Li records. Carbonate δ^7Li successions from Taşkent, Turkey and Takachiho, Japan are presented in this study, and carbonate δ^7Li values from the Shanggang and Shangsi sections in South China were presented in Cao et al. (2022). The locations of the siliciclastic δ^7Li records from New Zealand (Waiheke) and Svalbard (Festningen), discussed in comparison the carbonate record, are also shown (Rauzi et al., 2024). Paleogeographic map modified from Lau et al. (2017), with light gray representing reconstructed continental shelf.

2.1.1. Taşkent, Turkey

For this study, we measured Li isotopes in 34 carbonate samples from the Taşkent section, Turkey (fig. 3). The Taşkent stratigraphic section is in the western Taurus Mountains, 12 km southwest of the town of Taşkent in southern Turkey. The Taşkent section occurs within the Aladag Nappe, an allochthon thrust south over the autochthonous series of the Tauride block during the Eocene (Monod, 1997; Özgül, 1997). Taşkent strata were deposited within the interior of a vast shallow-marine carbonate platform developed on the Tauride block in the western Tethys seaway during the Permian and Early Triassic (Groves et al., 2005; Marcoux & Baud, 1986). Packages of siliciclastic shales and sandstones indicate that the shallow-marine

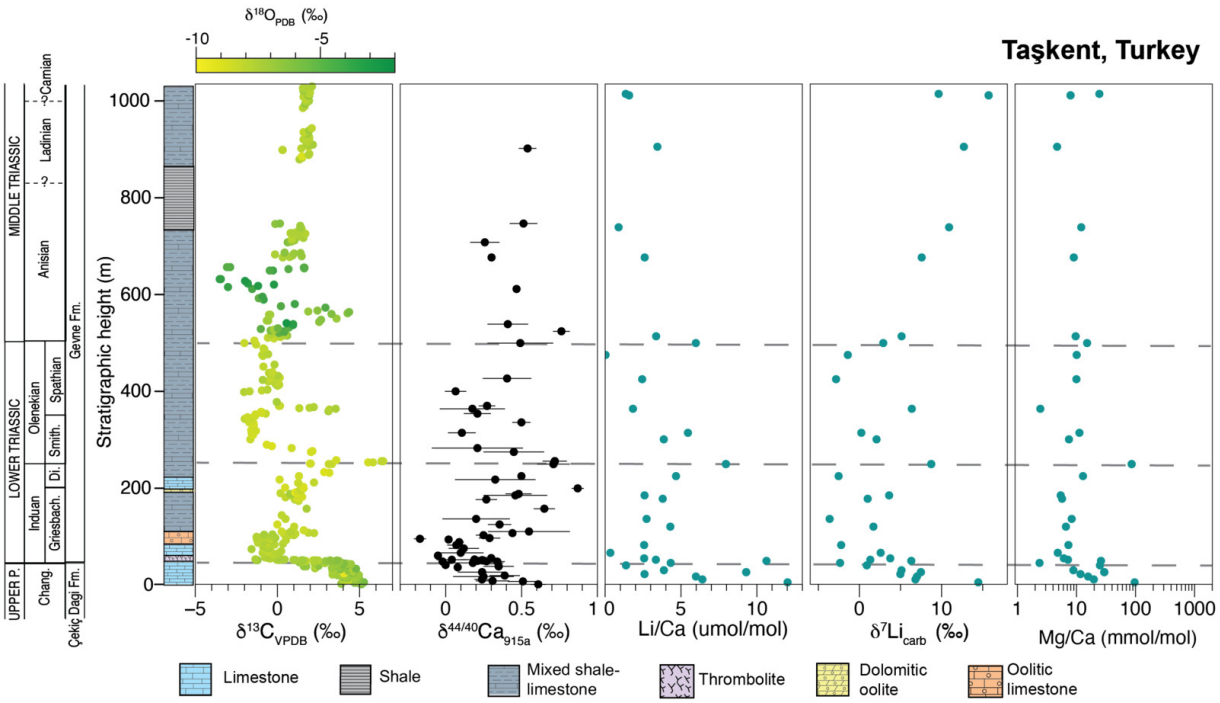

Figure 3. Stratigraphic column and geochemical data from Taşkent, Turkey. Stratigraphy, $\delta^{13}C$, $\delta^{18}O$, and $\delta^{44/40}Ca$ values are previously published (Lau et al., 2016, 2017). The Li/Ca ratios and $\delta^{7}Li_{carb}$ values are from this study. The $\delta^{7}Li_{carb}$ values are reported relative to LSVEC. Error bars for $\delta^{7}Li$ values (0.36‰; 2SD) are smaller than the symbols. Horizonal dashed lines indicate the time bins discussed in the text (Upper Permian, Induan, Olenekian, Middle to Late Triassic). Upper P. = Upper Permian, Chang. = Changhsingian, Di. = Dienerian, Smith = Smithian, U. Tr. = Upper Triassic. The boundaries between the Anisian, Ladinian, and Carnian stages of the Middle and Late Triassic are uncertain.

carbonate platform was attached to a landward source of siliciclastic sediments.

The Upper Permian strata of the Çekiç Dagi Formation consist of fossiliferous packstone and nodular wackestone with diverse marine fossils, including Changhsingian foraminifera (Altıner et al., 2024; Altıner & Özgül, 2001; Özgül, 1997; Ünal et al., 2003). The P/Tr boundary occurs in a 0.5 m-thick oolitic limestone, which is overlain by 1 m of microbialites (Payne et al., 2007). The lowermost Triassic contains a microbial-cemented crust of thrombolites, stromatolites, and arrays of aragonite fans interpreted to have precipitated on the seafloor (Baud et al., 1997, 2005). Sediments of the Lower Triassic continue within the Gevne Formation and contain oolites, micritic carbonates, and skeletal carbonate beds. The Middle to Upper Triassic facies in the upper Gevne Formation, which extend into the Carnian, contain intercalated carbonates and siliciclastics with oncolitic and skeletal limestones. Carnian strata are primarily debris flow conglomerates with allochthonous clasts.

2.1.2. Takachiho, Japan

For this study, we analyzed 26 carbonate samples from the Takachiho stratigraphic section in Japan (also called Kamura in other studies; fig. 4). The Takachiho section is located on the Chichibu terrane on the island of Kyushu (Payne et al., 2007). The Chichibu terrane is an allochthonous block that was accreted to a volcanic arc during the Cretaceous (Horacek et al., 2009). Shallow-marine carbonate sediments were deposited on a seamount in the Panthalassa Ocean that formed on a mid-ocean atoll complex during an upward-deepening succession (Horacek et al., 2009; Payne et al., 2007). Because of its isolated paleogeographic location, the input of terrigenous siliciclastic sediments was limited, and sediments are predominantly biologically derived carbonates (Musashi et al., 2001; F. Zhang, Algeo, et al., 2018; L. Zhang et al., 2019). Ages of the Changhsingian Mitai and Triassic Kamura Formations of the Takachiho section are constrained by conodont biostratigraphy (Sano & Nakashima, 1997; L. Zhang et al., 2019) and carbon isotope chemostratigraphy (Horacek et al., 2009). Spathian strata are mostly missing, most likely due to an unconformity (L. Zhang et al., 2019). However, the carbon isotope data of the measured section presented here captures the nadir of the N4 negative excursion (e.g., Song et al., 2014).

In the Takachiho section, sediments were initially deposited in an open-marine to shallow subtidal environment in the Late Permian, followed by a deepening-upward sequence with radiolarian and planktonic fossils predominant in the uppermost part of the section (Horacek et al., 2009; Payne et al., 2007; Sano & Nakashima, 1997). The Upper Permian Mitai Formation consists of massive, dolomitized, fusulinid-rich, skeletal wackestone-mudstone and is overlain by the Lower to Upper Triassic Kamura Formation. The P/Tr boundary occurs in a ~4 m-thick bed of dolomi-

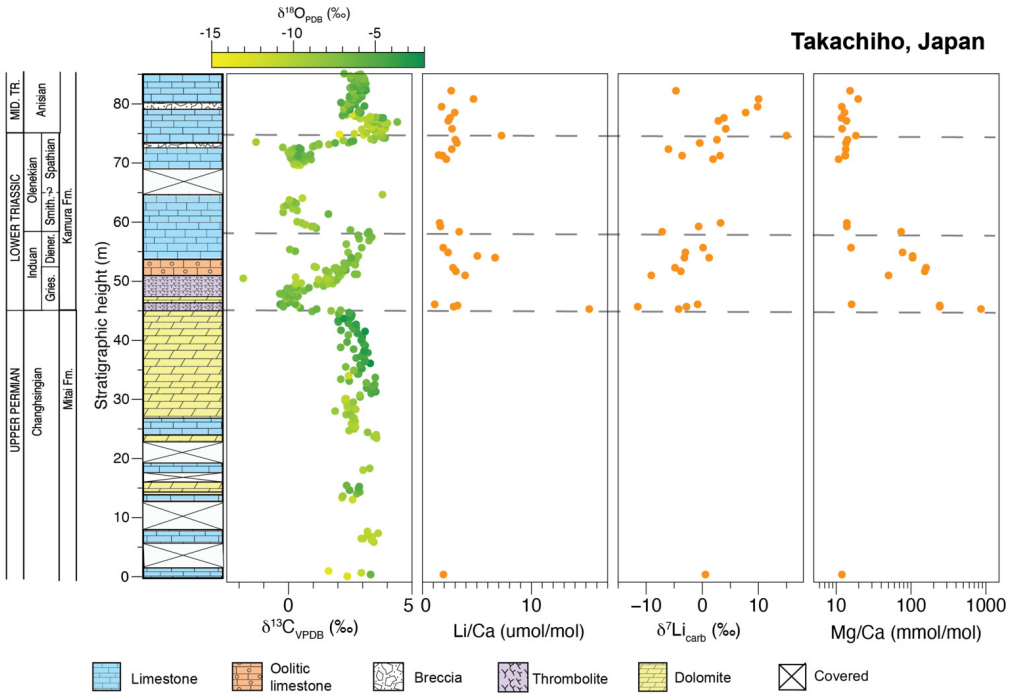

Figure 4. Stratigraphic column and geochemical data from Takachiho, Japan. The δ^7Li_{carb} values are reported relative to LSVEC. Note that Spathian strata are not continuous (L. Zhang et al., 2019) with an arbitrary interval of cover marked here, and units assigned to the Spathian are based on carbon isotope chemostratigraphy (the N4 carbon isotope excursion of Song et al., 2014). Error bars for δ^7Li values (0.58‰; 2SD) are smaller than the symbols. Horizonal dashed lines indicate the time bins discussed in the text (Upper Permian, Induan, Olenekian, Middle Triassic). Gries. = Griesbachian, Diener. = Dienerian, Smith. = Smithian, Mid. Tr. = Middle Triassic.

tized calcimicrobial framestone (Payne et al., 2007; Sano & Nakashima, 1997), which is overlain by 2 m of oncolitic grainstone followed by ~16 m of bivalve-rich wackestone to grainstone that composes the rest of the middle member of the Kamura Formation. The middle member of the Kamura Formation contains several karst-derived breccia units (Sano & Nakashima, 1997). The absence of Spathian conodonts and the presence of breccias above the Smithian units suggest an unconformity lasting for much of the Spathian substage (L. Zhang et al., 2019). In the Takachiho section, carbon isotope chemostratigraphy suggests that ~3 m of Spathian wackestone is exposed, which is overlain by ~12 m of fossiliferous wackestone of the Middle Triassic.

2.2. Analytical Methods

2.2.1. Carbon, oxygen, calcium isotope, and carbonate content data

Carbon, oxygen, and calcium isotope data for Taşkent were previously published by Payne et al. (2007) and Lau et al. (2016, 2017) and sample preparation and analytical methods are described therein. Carbon and oxygen isotope data for Takachiho, Japan, were analyzed for this study at Harvard University. Micrite was selectively drilled from samples using a 0.8 mm diamond or tungsten carbide dental drill bit. Samples were reacted with concentrated phosphoric acid at 90 °C in a common acid bath and then measured on a dual inlet mass spectrometer (VG Optima). Isotope ratios are reported in standard delta notation relative to V-PDB and analytical precision was ± 0.1‰ (2σ) based on replicate analyses of a laboratory standard.

Carbonates from Takachiho, Japan were deposited in an atoll far from continental sources (L. Zhang et al., 2019). Conversely, samples from Taşkent contain varying proportions of carbonate and siliciclastic sediments. To consider the effect of siliciclastic contributions, we report carbonate content for the Taşkent samples. Samples were analyzed in the Stable Isotope Biogeochemistry Laboratory at Stanford University with a Finnegan MAT252 mass spectrometer coupled to a Kiel III carbonate device. Between 50 and 100 µg of limestone powder was reacted in phosphoric acid (H_3PO_4) at 70 °C for 600 seconds. Estimates for carbonate content for Taşkent samples were made using a k-factor approach, which includes the sample mass and the pressure of the sample measured by the Kiel III carbonate device. The results from unknowns were compared to the theoretical weight percent of the NBS-19 standard (100%). The accuracy of this approach is limited by the ability to accurately weigh small quantities of sample and accordingly the uncertainty is estimated to be 5–10%.

2.2.2. Lithium isotopes

Carbonate-based proxies may be biased by contamination from non-carbonate phases (e.g., Cao et al., 2023). To avoid this, samples were prepared following the methods of Dellinger et al. (2020) and Kalderon-Asael et al. (2021). Rock chips with minimal veining and of relatively homoge-

nous color were selected for sampling. Approximately 200 mg of powder was collected with a microdrill with a diamond or tungsten carbide drill tip, avoiding veins and heterogeneous surfaces. Sampling of visible skeletal grains was minimal, avoiding potential vital effects and inter-species variability (Dellinger et al., 2018). Samples were dissolved following Dellinger et al. (2020) and Kalderon-Asael et al. (2021). Approximately 200 mg of powder was weighed into a 50 mL acid-washed centrifuge tube and pre-washed with 26.67 mL of 1 M ammonium acetate to remove ions adsorbed on siliciclastic particles. After 30 minutes, the supernatant was removed by centrifugation and the sample was then washed with 13.33 mL of ultrapure water. Following centrifugation once again, the supernatant wash was removed. A stepwise dissolution procedure was used to limit the possibility of contamination from clay particles. Three consecutive dissolution steps were performed, where 13.33 mL of 0.05 N distilled hydrochloric acid (HCl) was added to each sample, sonicated for 10 minutes, allowed to react for 4 hours, 2 hours, and 10 minutes, respectively, and then centrifuged with the collection of the supernatant from each step. The supernatant from all three dissolution steps were combined for geochemical analysis.

For Taşkent samples, trace element analysis of Li, Al, Ca, Mg, Sr, and Mn was performed using the Thermo Scientific Element XR ICP-MS at the Yale Metal Geochemistry Center. For Takachiho samples, trace element analysis for Li, Mg, Sr, and Mn was performed with a Thermo Scientific iCAP TQ ICP-MS, and analysis of Al and Ca was performed with a Thermo Scientific iCAP 7400 ICP-OES in the Laboratory for Isotopes and Metals in the Environment (LIME) at Penn State. Compared to carbonate minerals, clays have a much higher concentration of Li and preferentially adsorb ^{6}Li. To ensure minimal Li contributions from clay, Al/Ca ratios were used to screen the leached samples. Samples with Al/Ca ratios > 0.8 mmol/mol (Kalderon-Asael et al., 2021; Pogge von Strandmann et al., 2013) were excluded from further processing due to the likelihood of clay contamination. Of the remaining sample subset, samples with at least 5 ng of Li were identified. For these samples, Li was isolated from other matrix elements using column chromatography. Samples were redissolved in 0.2 mL of 0.2 N HCl. 2.0 mL of Bio-Rad AG50W-X12 200–400 mesh resin was added to columns and washed with 6.0 mL 6 N HCl and ultrapure water twice each before conditioning with 6 mL of 0.2 N HCl. After the sample was loaded onto the column, the matrix elements were eluted with 10 mL of 0.2 N HCl. Next, Li was collected by stepwise addition of a total of 25 mL of 0.2 N HCl. Hydrogen peroxide (H_2O_2) and, subsequently, concentrated nitric acid (HNO_3), was added to dried samples to remove residual organics from the resin. After drying down to completion, samples were dissolved in 1 mL of 2% HNO_3 for analysis.

Because Li is fractionated during column chromatography, yields of ~100% are necessary. Yield checks were performed on all samples and two standards before Li isotope analysis by collection, combination, and concentration analysis of 2 mL of solution before and after the expected Li elution. On average, yields were > 99% and the median yield was 99.1%. Accuracy was further confirmed by processing standards through column chemistry and comparing to published values (table S2; described below). Lithium isotope ratios for Taşkent samples were analyzed with a Thermo Fisher Scientific Neptune Plus Multiple-Collector ICP-MS (MC-ICP-MS) at the Yale Metal Geochemistry Center, and Li isotopes for Takachiho were analyzed with a Neptune Plus MC-ICP-MS in LIME. An Aridus II desolvating nebulizer was used to aspirate samples. The bracketing standard for Li isotope ratios from Taşkent is the commonly used LSVEC standard. The bracketing standard for the Takachiho samples is IRMM-016, which is similar in composition to LSVEC and within typical measurement error ($\delta^7Li_{IRMM\text{-}016}$ - δ^7Li_{LSVEC} = −0.2 ± 0.3‰, Tomascak et al., 2016) (table S2). Delta values are reported as δ^7Li_{LSVEC} = 1000 x ($^7Li/^6Li_{sample}/^7Li/^6Li_{LVSEC}$ − 1) (i.e., a 0.2‰ offset is applied to Takachiho samples that were bracketed with IRMM-016). The LSVEC standards (accepted value = 0‰) processed in this study exhibited mean δ^7Li values of 1.33 ± 1.77‰ (2SD; n=2) in LIME and 0.46 ± 0.07‰ (n=2) at Yale. IAPSO Atlantic seawater standards processed in this study yielded a mean δ^7Li value of 30.45 ± 0.42‰ (2SD; n=2) at LIME and a value of 31.45 ± 0.07‰ (n=2) at Yale (table S2), which is in good agreement with previous studies (30.88 ± 0.12‰; Huang et al., 2010). In LIME, reproducibility was gauged by repeated measurements of SRM-3129a and reported as 1.55‰ (2SD; n=19) and by repeated measurements of the bracketing standard as 0.58‰ (2SD; n=19) (tables S1, S2). The analyzed δ^7Li of SRM-3129a was 6.75‰, within error of the long-term value of 6.45 ± 0.60‰ in LIME (2SD, n= 30) (table S2). Samples from Takachiho were run in duplicate with the average reported in table S1. In total, four duplicates from powder were prepared and produced an average difference in δ^7Li of 2.2‰. Uncertainty is reported as the reproducibility (2SD) of the bracketing standard and was 0.36‰ at Yale and was 0.58‰ in LIME.

3. RESULTS

3.1. Taşkent, Turkey

The mean Li concentration of all samples from Turkey is 0.18 ppm (n=35) and ranges from 2 ppb to 0.54 ppm (table S1). Concentrations in the Changhsingian average 0.20 ppm (n=8) and are slightly lower in the remainder of the section, averaging 0.16 ppm, 0.18 ppm, and 0.14 ppm in the Induan (n=10), Olenekian (n=9) and Anisian (n=8), respectively. Mean Li/Ca ratios decrease from 5.73 µmol/mol in the Changhsingian (n=8) to 3.75, 4.06, and 2.94 µmol/mol in the Induan (n=10), Olenekian (n=9), and Anisian–Carnian (n=8), respectively (figs. 3, 4, table S1). There is no significant difference in Li concentration or Li/Ca ratio when compared by stage (e.g., ANOVA p-value > 0.05; table S1 and fig. 5). The mean Al/Ca ratio (mmol/mol) is 0.22 (n=35).

Carbonate samples exhibit a mean δ^7Li value of 5.5±9.9‰ (n=8) in the Changhsingian and decrease to 1.2±6.3‰ (n=10) in the Induan, reaching the lowest value of −3.6‰ at 134.8 m stratigraphic height in the Griesbachian (fig. 3). The δ^7Li values increase to an average of

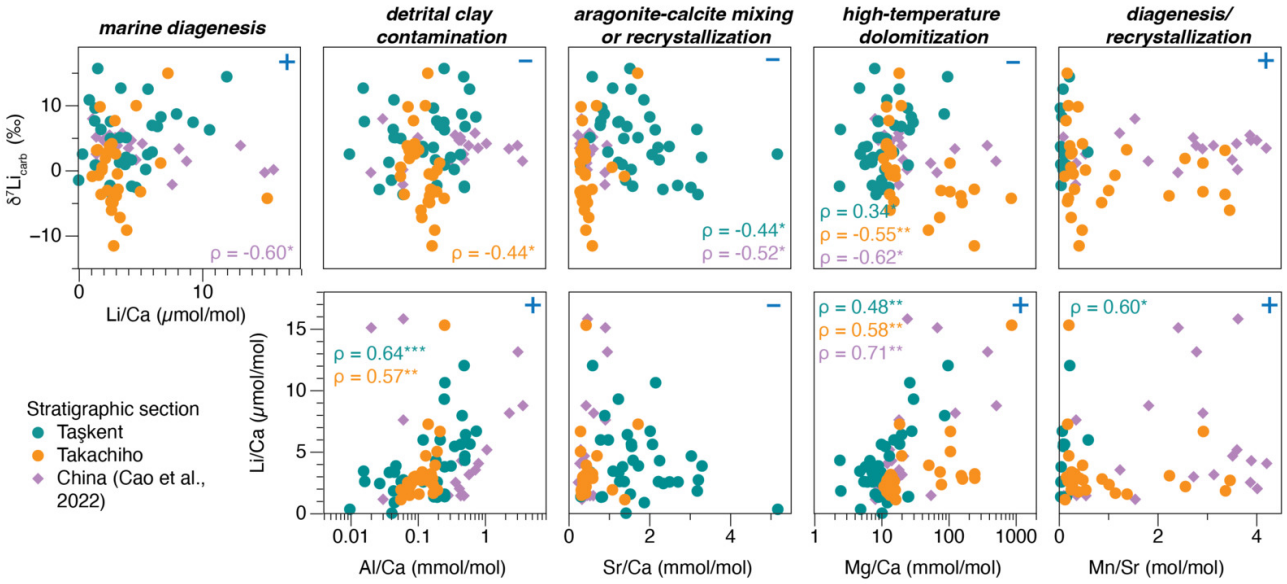

Figure 5. Crossplots of carbonate δ^7Li values (top) and Li/Ca ratios (bottom) against elemental ratios. Data from three carbonate sections are compared: two from this study (Taşkent and Takachiho) and previously published data from South China (Cao et al., 2022). Note that Al/Ca and Mg/Ca ratios are plotted on a logarithmic scale. Blue '+' or '-' symbols in the upper right corner indicate whether positive or inverse correlations are expected for different factors, described by the column headers. For example, contamination by detrital clay with low δ^7Li and high [Li] (second column) is expected to result in an inverse correlation between δ^7Li and Al/Ca. The negative correlation between δ^7Li and Mg/Ca could be related to a large negative isotope fractionation determined from high-temperature dolomite replacement experiments (Taylor et al., 2019). If a significant correlation is observed for the data from a stratigraphic section, the Spearman's ρ is noted where the color depicts the section and *p*-values are denoted where * = <0.05, ** < 0.01, and * < 0.001 (see table S4).**

2.6±7.4‰ (n=9) in the Olenekian. In the Anisian–Carnian, δ^7Li values increase steadily to a mean of 10.6±5.8‰ (n=8) in the Middle to Upper Triassic samples. When grouped by stage, these differences are statistically significant (ANOVA *p*-value < 0.001; fig. S1). Specifically, δ^7Li values from the Middle to Late Triassic are significantly higher than those of the Changhsingian, Induan, or Olenekian (evaluated using Tukey-Kramer post-hoc test, function *TukeyHSD* in base *stats* package in *R,* R Core Team, 2024; table S3).

3.2. Takachiho, Japan

The Li concentrations range from 0.05 to 0.32 ppm (n=29; table S1). The single Changhsingian sample has a Li concentration of 0.09 ppm and average values are relatively invariant afterward, with mean concentrations of 0.14 ppm (n=8) and 0.09 ppm (n=10) in the Induan and Olenekian, respectively. The Li/Ca ratios are highest in the Induan with an average value of 4.87 μmol/mol (n=8) and remain elevated throughout the Olenekian (2.41 μmol/mol, n=10) and the Anisian (3.31 μmol/mol, n=10) (fig. 4, table S1). There is no significant difference in Li concentration or Li/Ca ratio when compared by stage (e.g., ANOVA p-value > 0.05; fig. 5). The average Al/Ca ratio (mmol/mol) is 0.13 (n=29).

The single Changhsingian sample from this section has a δ^7Li value of 0.6‰ (fig. 4). In the Induan, δ^7Li values decrease to an average of −4.5±8.3‰ (n=8). In the Olenekian, mean δ^7Li values increase to −1.5±7.3‰ (n=10). In the Anisian, the average δ^7Li value rises to 5.1±11.4‰ (n=10), reaching a maximum of 15.0‰. Similar to Taşkent, differences in mean value are statistically significant when the δ^7Li data are grouped by stage (ANOVA *p*-value < 0.001; table S3). The δ^7Li values of Anisian samples are also significantly higher than that of samples from the Induan or the Olenekian (Tukey-Kramer post-hoc test; table S3 and fig. S1). However, the δ^7Li value of the Changhsingian is represented by only one sample from this section.

3.3. Correlation statistics

We performed a Spearman's rho ranked correlation test (function *cor.test*, method = "*spearman*", in the base *stats* package) to determine the significance of the correlations of elemental ratios (Al/Ca, Sr/Ca, Mg/Ca, and Mn/Sr) with Li/Ca ratios and δ^7Li values for the Turkey (Taşkent) and Japan (Takachiho) datasets (fig. 5; table S4). Although Al/Ca ratios are low for both sections, there is a moderate to strong, positive correlation (Spearman's ρ = 0.64) between Al/Ca and Li/Ca ratios at Taşkent with a high statistical significance (p-value < 0.001) but no correlation with δ^7Li value. At Takachiho, a moderate, negative correlation between δ^7Li value and Al/Ca ratio is indicated (Spearman's ρ = −0.44 and p-value = 0.02). Similarly, Li/Ca and Al/Ca ratios are positively correlated (Spearman's ρ = 0.57 and p-value < 0.01). At Taşkent and Takachiho, there is a minor to moderate correlation between δ^7Li values and Mg/

Ca ratios, although the correlation is positive at Taşkent (Spearman's ρ = 0.34 and p-value 0.04) and negative and Takachiho (Spearman's ρ = −0.55 and p-value < 0.01). A negative correlation between δ^7Li values and Mg/Ca ratios also occurs in previously published data from South China (Spearman's ρ = −0.62 and p-value = 0.01; Cao et al., 2022). In both sections of this study and in South China, there is a positive correlation between the Li/Ca and Mg/Ca ratios (table S4).

4. DISCUSSION

4.1. Evaluating siliciclastic contamination on the Turkey and Japan carbonate δ^7Li records

Carbonates are relatively depleted in Li compared to silicate minerals, leading to the development of a weak-acid chemical leaching method designed to dissolve carbonates while retaining silicates in the residual solid load (Nadeau et al., 2025; Pogge von Strandmann, Schmidt, et al., 2019; Yin et al., 2023). Silicate contamination of carbonate leachates was initially assessed using the Al/Ca concentration of leachates. Aluminum is enriched in silicates relative to carbonates, and previous work has established a maximum acceptable Al/Ca concentration of carbonate leachates of 0.8 mmol/mol (Kalderon-Asael et al., 2021; Pogge von Strandmann et al., 2013). All Al/Ca ratios of samples measured here fall below this threshold, with average Al/Ca ratios of 0.13 (n=28) and 0.21 (n=21) for Takachiho and Taşkent, respectively.

Correlation between Li/Ca and Al/Ca can provide insight into silicate contamination of carbonate leachates due to the enrichment of Al and Li and depletion of Ca in silicates relative to carbonates. Cross plots comparing δ^7Li, Li/Ca, Sr/Ca, and Mg/Ca are shown in figure 5. At Taşkent, the positive correlation between Al/Ca and Li/Ca ratios may suggest the effects of contamination, however, no correlation is observed between δ^7Li values and either ratio (fig. 5). At Takachiho, δ^7Li values are inversely correlated with Al/Ca ratios, and Li/Ca and Al/Ca ratios are positively correlated (fig. 5). Although this pattern may indicate that contamination by siliciclastic material contributed to the lowest δ^7Li values in Takachiho in the Triassic, the range in the Al/Ca ratios is small compared to other sections, with variations within an order of magnitude. As discussed in the geologic setting, Takachiho was deposited in a carbonate atoll distal from any continental sources (L. Zhang et al., 2019), making siliciclastic input to this site limited.

Another line of evidence to determine siliciclastic contamination is the relationship between δ^7Li value and Li/Ca ratio, as siliciclastic materials have a higher Li concentration than carbonates (Dellinger et al., 2020; Vigier et al., 2007). There is no statistically significant covariation between δ^7Li value and Li/Ca ratio at Takachiho (table S4), which supports a lack of detrital contamination. The potential for detrital contribution at Takachiho, as an isolated seamount, is extremely low, with sedimentation dominated by biogenic carbonate. The potential for detrital contamination is higher at Taşkent, which represents a mixed carbonate-clastic ramp in the Lower Triassic. However, there are no relationships observed between wt.% $CaCO_3$ and δ^7Li values, the uncertainty on δ^7Li values, Li/Ca ratio, or Li concentration (fig. S3; see Nadeau et al., 2025). We also do not observe a relationship between wt.% $CaCO_3$ and Al/Ca ratio (fig. S3), and stratigraphic trends in δ^7Li values at Taşkent are not a result of stratigraphic changes in wt.% $CaCO_3$ and there are no correlations with the facies type sampled (fig. S4). Therefore, while we cannot fully rule out contamination, there is no evidence to indicate a systematic effect on the data that are presented in this study.

4.2. Evaluating diagenetic alteration on the Turkey and Japan carbonate δ^7Li records

We observe a gradual but consistent trend toward higher δ^7Li values in the Middle Triassic in both the Paleo-Tethys (Turkey) and in the Panthalassic (Japan) Oceans (figs. 3, 4). A positive shift in spatially disparate sections suggests that this feature is not driven by local processes, including diagenesis, but this possibility must be considered, as even carbonates free of siliciclastic debris can have δ^7Li signals that are not reflective of the marine chemistry at the time of deposition due to diagenetic alteration. Recent studies have concluded that stratigraphic trends in carbonate δ^7Li from diverse time intervals and carbonate lithologies (limestone, dolostone) reflect different styles of diagenesis (Crockford et al., 2021; Dellinger et al., 2020; Murphy et al., 2022; Nadeau et al., 2025; W.-Q. Wang et al., 2024). Here, we consider the potential effects of diagenesis on the carbonate δ^7Li record from the Taşkent and Takachiho sections. Studies of δ^7Li values in shallow-marine carbonate sediments from the Great Bahama Bank, the Key Largo limestone, and the South China Sea demonstrated that the style of diagenesis results in different degrees and direction of alteration for δ^7Li values and Li/Ca ratios (Dellinger et al., 2020; Wei et al., 2023).

The average δ^7Li value of meteorically altered carbonates in the South China Sea generally preserves a primary (e.g., seawater) δ^7Li value (Wei et al., 2023). Wei et al. (2023) use this example to argue that sediment-buffered diagenesis—in scenarios where the diagenetic fluid was meteoric water—is expected to best preserve the initial δ^7Li value, thereby representing variations in (local) seawater δ^7Li value. They attribute the preservation of the primary signal to the low Li concentration of groundwater in these samples. However, carbonates from the Great Bahama Bank that experienced meteoric water diagenesis exhibited non-primary δ^7Li values, significantly lower than seawater, that were attributed to variability in the δ^7Li values of groundwater (Dellinger et al., 2020). Therefore, meteoric diagenesis must be considered as a potential explanation for the very low Permian and Lower Triassic carbonate δ^7Li values. This consideration is important at Taşkent, where mixed shale-limestone facies indicate a shallow carbonate platform with terrestrial influences, including the potential for meteoric waters to affect the geochemistry at this location. However, several lines of evidence point to the absence of significant meteoric water diagenesis at Taşkent. For example, low δ^{18}O values are indicative of influence by mete-

oric water; samples with anomalously low $\delta^{18}O$ values that are near the Spathian–Anisian contact, which has been proposed to be due to shallowing and meteoric diagenesis of these strata (Lau et al., 2017), were avoided in this study. The remainder of the $\delta^{18}O$ values in this section do not exhibit stratigraphic trends that suggest meteoric influence (Lau et al., 2017). Additionally, there is no sedimentological evidence for meteoric diagenesis (meteoric cements, etc.) at Taşkent (Payne et al., 2007). Therefore, we do not find evidence that meteoric diagenesis had a major impact on these samples.

Early marine diagenesis has also been argued to result in alteration of the $\delta^{7}Li$ signal (e.g., Dellinger et al., 2020; Murphy et al., 2022; Wei et al., 2023). Calcium isotope records can be used to identify sediment- *vs*. fluid-buffered diagenesis, with seawater-buffered diagenesis of aragonite to low-magnesian calcite resulting in higher $\delta^{7}Li$ values and lower Li/Ca ratios (Crockford et al., 2021; Dellinger et al., 2020; Murphy et al., 2022; Nadeau et al., 2025; Wei et al., 2023). This observation has been explained by differences in the Li isotope fractionation and partition coefficient for aragonite and calcite, as well as the potential for a smaller isotope fractionation factor between porewater and diagenetic carbonate resulting from near-equilibrium recrystallization (Dellinger et al., 2020; Wei et al., 2023). Numerical modeling supports this framework (Crockford et al., 2021; Murphy et al., 2022). However, it should be noted that the assumed diagenetic Li isotope fractionation of ~0‰ is inferred from data from Neogene to Recent carbonate sediments (e.g., Dellinger et al., 2020), and this assumption for fluid-buffered alteration is generally applied to dolomitizing diagenesis (Crockford et al., 2021; Murphy et al., 2022; Nadeau et al., 2025). The effects of dolomitization on $\delta^{7}Li$ values are not well constrained (see further discussion in the following section), meaning that there remains uncertainty behind the mechanisms underlying the effects of marine diagenesis on carbonate $\delta^{7}Li$ values.

In many studies, significant carbonate diagenetic alteration has been identified by comparing elemental ratios, such as Li/Ca, Sr/Ca, and Mn/Sr, with $\delta^{7}Li$ values (fig. 5, tables S1 and S2; Dellinger et al., 2020; Kalderon-Asael et al., 2021; Krause et al., 2023). In this assessment, linear covariations are not expected, but correlations between $\delta^{7}Li$ and these elemental ratios can be used to identify first-order effects of diagenesis (as is suggested by diagenetic modeling predictions; Murphy et al., 2022). Such correlations can be statistically determined using rank correlation tests such as Spearman's rho. For example, an inverse correlation between $\delta^{7}Li$ value and Sr/Ca ratio can reflect the depletion of Sr during the transition from aragonite to calcite under fluid-buffered conditions (Dellinger et al., 2020; Wei et al., 2023). Although no significant covariation between $\delta^{7}Li$ value and Sr/Ca ratio occurs in the Takachiho data (Spearman's ρ in table S3), a significant inverse relationship is present at Taşkent (Spearman's ρ = -0.44, *p*-value = 0.01), driven by one sample with a high Sr/Ca ratio and high $\delta^{7}Li$ value (fig. 5). To account for multiple effects, we also use a generalized linear model (function *glm* in R; table S5) of $\delta^{7}Li$ value versus location, stage, and elemental ratios (Sr/Ca, Li/Ca, Mg/Ca, Mn/Sr) as predictor variables; these results demonstrate that the stratigraphic increase in the Anisian cannot be solely attributed to a mineralogical effect (as represented by Sr/Ca and Mg/Ca ratios) or diagenesis (Mn/Sr ratios).

The influence of diagenesis on $\delta^{7}Li$ values at Taşkent can also be assessed by comparing $\delta^{7}Li$ and $\delta^{44/40}Ca$. Comparison of $\delta^{7}Li$ with $\delta^{44/40}Ca$ and $\delta^{26}Mg$ values (the latter more relevant for dolomites) have been used to determine whether stratigraphic variations in carbonate $\delta^{7}Li$ values were produced by sediment- and fluid-buffered diagenesis. For instance, neomorphism of aragonite sediments from cores from the Bahamas resulted in a positive correlation between $\delta^{7}Li$ and $\delta^{44/40}Ca$ values and an inverse relationship with Sr/(Ca+Mg) ratios (Murphy et al., 2022). Because higher $\delta^{44/40}Ca$ values are interpreted as representative of increasing alteration during recrystallization/neomorphism and specifically fluid-buffered alteration, this test was used to demonstrate that stratigraphic intervals with higher $\delta^{7}Li$ values in some cores represent diagenetic influence, not changes in seawater composition. Similarly, a positive correlation between $\delta^{7}Li$ and $\delta^{44/40}Ca$ values in Tonian carbonates that are interpreted to have been dolomitized very early after formation, based on field observations, are used to argue that the stratigraphic increases in $\delta^{7}Li$ value are not representative of changes in seawater $\delta^{7}Li$ signature but instead result from diagenetic processes (Crockford et al., 2021). The altered carbonate $\delta^{7}Li$ value from fluid-buffered diagenesis is argued to approximate that of the diagenetic fluid—and therefore constrains the seawater $\delta^{7}Li$ signature, assuming this is the diagenetic fluid. This approach has been used to estimate Tonian (Crockford et al., 2021), Cretaceous (Nadeau et al., 2025), and Miocene seawater $\delta^{7}Li$ values (Murphy et al., 2022). In both examples, it is argued that the most altered samples—interpreted to have occurred under the influence of seawater—can be used to reconstruct the seawater $\delta^{7}Li$ signature if it assumed that the isotopic fractionation during recrystallization is near 0‰ (Crockford et al., 2021; Murphy et al., 2022).

Published $\delta^{44/40}Ca$ values and Sr/Ca ratios (n=60) for the Taşkent section, which includes 18 samples that were also analyzed for Li isotopes in this study, are relatively low and high respectively (fig. 3), characteristic of sediment-buffered diagenesis and aragonite as the predominant initial $CaCO_3$ polymorph (Lau et al., 2017). Although variability in the $\delta^{44/40}Ca$ value is generally most representative of diagenesis (fig. 3; Fantle et al., 2020; Fantle & DePaolo, 2007; Fantle & Higgins, 2014), it is possible that stratigraphic shifts in the carbonate $\delta^{44/40}Ca$ value can record Ca cycle perturbations (e.g., Gussone et al., 2020). It is important to note that the negative $\delta^{44/40}Ca$ excursion at the P/Tr boundary (but not changes in $\delta^{44/40}Ca$ in the Early and Middle Triassic) has been reproduced at multiple shallow carbonate sections across the Tethys Ocean as well as in conodont apatite, though the exact mechanism underlying this shift is debated (Hinojosa et al., 2012; Komar & Zeebe, 2016; Payne et al., 2010; Silva-Tamayo et al., 2018; J. Wang et al., 2019). If the most negative $\delta^{44/40}Ca$ values at the P/

Tr boundary (see fig. 3) are ignored for this reason, we see that the $\delta^{44/40}Ca$ values are relatively high at ~200 m and from 500 to 900 m. In contrast, the carbonate $\delta^{7}Li$ record at this site does not exhibit clear stratigraphic changes from 100 to 500 m, whereas $\delta^{7}Li$ values increase more systematically above 500 m. Therefore, unlike the Tonian $\delta^{44/40}Ca$, $\delta^{7}Li$, and $\delta^{13}C$ record (Crockford et al., 2021), the absence of obvious stratigraphic covariation does not indicate synchronous shifts in the style and extent of diagenesis as the primary factor driving geochemical trends. This is also supported by the crossplot of $\delta^{7}Li$ vs. $\delta^{44/40}Ca$ data analyzed from the same samples (fig. 6). In comparison to other carbonate $\delta^{7}Li$ and $\delta^{44/40}Ca$ datasets that are interpreted to be primarily driven by diagenesis (e.g., Crockford et al., 2021; Murphy et al., 2022), the samples from Taşkent are also positively correlated (Spearman's $\rho = 0.57$, p-value = 0.02). Given the nature of the extinction (e.g., Nsingi et al., 2025), it is possible that these could reflect actual stratigraphic changes (i.e., lower $\delta^{7}Li$ and lower $\delta^{44/40}Ca$ values in the Induan but higher $\delta^{7}Li$ and higher $\delta^{44/40}Ca$ values in Late Permian and Anisian), but this relationship could also indicate the role of diagenesis. However, unlike these other datasets, the Taşkent $\delta^{7}Li$ and $\delta^{44/40}Ca$ records show no relationship with Sr/Ca ratios, as would be expected if diagenetic alteration explained these trends (fig. 6; see Murphy et al., 2022). Further, the fact that some of these samples have retained these geochemical signatures during recrystallization (instead of being altered to high $\delta^{44/40}Ca$ values and low Sr/Ca ratios), and the relatively low Mn/Sr ratios (fig. 5), suggest sediment-buffered preservation of primary $\delta^{7}Li$ signatures is likely at Taşkent.

Though there are fewer constraints on Takachiho (i.e., no $\delta^{44/40}Ca$ values), the $\delta^{13}C$ chemostratigraphy of the Early Triassic—a globally reproducible feature, with characteristic negative and positive isotope excursions (e.g., Payne et al., 2004)—is generally preserved (fig. 4). This observation supports limited fluid-buffered diagenesis, at least with respect to $\delta^{13}C$ values, a relatively well-buffered system. Uranium isotopes, which are thought to be less sensitive to diagenesis than $\delta^{7}Li$ values but more sensitive than $\delta^{13}C$ values, have been analyzed in the Kamura Formation, in Taşkent, and in other sections in South China (Lau et al., 2016; F. Zhang, Algeo, et al., 2018). The records are comparable in absolute value. At this section, the Mn/Sr ratios are generally low, with a maximum of 3.4 (mol/mol), though a significant inverse relationship between Mn/Sr ratios and $\delta^{7}Li$ values occurs at this site (table S3). Samples with high Mn/Sr ratios also have lower $\delta^{7}Li$ values (fig. 5), but most samples with low $\delta^{7}Li$ values also have low Mn/Sr ratios (i.e., <0.4 mol/mol; fig. S5). Therefore, we interpret these datasets to imply that alteration did not systematically bias the stratigraphic $\delta^{7}Li$ trends observed at this section.

In summary, sediment-buffered diagenesis is inferred for the carbonates from Takachiho and Taşkent based on a lack of correlation between $\delta^{7}Li$ values and Li/Ca or Sr/Ca ratios. Diagenetic alteration, potentially by a non-seawater fluid, however, is more prevalent at Takachiho based on higher Mn/Sr ratios, which could have resulted in lower $\delta^{7}Li$ values in at least some of the samples (discussed further below). We do not find evidence that meteoric diagenesis is responsible for the stratigraphic trends—meaning, this process did not result in a systematic bias in the carbonate $\delta^{7}Li$ records. The scatter in both records likely reflects variable, but non-systematic, diagenetic influences as is observed in modern platform carbonates (Dellinger et al., 2020; Wei et al., 2023). With the available $\delta^{44/40}Ca$ data from Taşkent, it is possible that the trend to increasing $\delta^{7}Li$ values in the Middle to Late Triassic could reflect a shift from sediment-buffered to fluid-buffered diagenesis (fig. 6). If true, carbonate $\delta^{7}Li$ values are ~20‰ lower than modern seawater and well outside the bounds of any known process that would impact Li isotope fractionation, indicating a substantially different Li isotope mass balance compared to today.

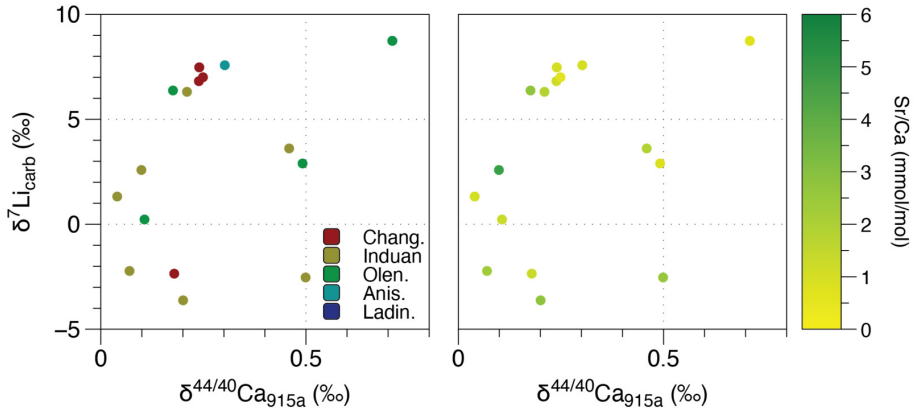

Figure 6. Crossplots of paired $\delta^{7}Li$ vs. $\delta^{44/40}Ca$ data collected from the same samples from Taşkent. Ca isotope data are from Lau et al. (2017). In left, datapoints are colored by stage (Chang.=Changhsingian; Olen.=Olenekian; Anis.=Anisian; Ladin.=Ladinian). In right, datapoints are colored by Sr/Ca ratio. These data are significantly correlated (Spearman's $\rho = 0.57$, p-value = 0.02).

4.3. Differences in the P/Tr carbonate δ^7Li record among sites

The new carbonate δ^7Li values from this study generally reproduce the patterns observed in a stratigraphic record that suggests enhanced reverse weathering in the Late Permian and Early Triassic (Cao et al., 2022). Carbonate δ^7Li records from two stratigraphic sections (Shangsi and Shanggang) in the eastern Paleotethys, located in present-day South China, are interpreted to capture changes in the seawater δ^7Li signature during the latest Permian and Early Triassic (Cao et al., 2022). Because a comparable weak acid leach was employed in this study, these data are compared with the records presented here (figs. 7, S2). The δ^7Li record from Meishan covered a condensed interval across the Permian–Triassic boundary (H. Sun et al., 2018). These samples were prepared using a whole-rock dissolution of basinal carbonate rocks and a correction for the siliciclastic contribution was applied to estimate the seawater δ^7Li value. Because this correction comes with substantial uncertainty, we do not include this dataset in the following discussion.

In all three sections, which cover the Eastern Tethys (South China), Western Tethys (Taşkent), and the Panthalassa Ocean (Takachiho), carbonate δ^7Li values are consistently near or below 0‰ at the Permian/Triassic boundary, remain low through the Induan, and increase in the Olenekian (fig. 7A). The δ^7Li values in the Middle Triassic are significantly higher than in the Late Permian or Early Triassic. The overall consistency and general reproducibility in stratigraphic patterns suggest a non-localized trend in the combined carbonate records. Because previously published records from South China do not extend to the Anisian, the finding in our study that δ^7Li values increase substantially in the Middle Triassic is notable.

However, there are key differences among the three records. First, there is a large range in δ^7Li values from Lower Triassic samples spanning −10‰ (Takachiho) to ~+8‰ (Taşkent). The δ^7Li values of samples from Takachiho are significantly lower than those of coeval samples from Taşkent and South China (table S6). Second, the lowest δ^7Li values in Taşkent and Takachiho are in the Induan, whereas the lowest δ^7Li values in the South China sections occur below the Permian/Triassic boundary. The significance of the differences in where these minima occur relative to the Permian/Triassic boundary is unclear; the Changhsingian is only represented by one sample at Takachiho and the Taşkent record is concentrated in the uppermost Permian. There are several processes that can result in carbonate δ^7Li values that are non-reflective of a global seawater δ^7Li signature. Spatial variability in carbonate δ^7Li values could be due to *(1)* a heterogeneous seawater δ^7Li signature, *(2)* a variable fractionation factor from seawater due to differences in carbonate mineralogy, diagenesis, or formation water pH, and/or *(3)* variable contamination from clays, occurring inconsistently in these sections. We discuss heterogeneous seawater δ^7Li signatures in Section 5; below, we explore the other possible explanations.

Various carbonate mineralogies exhibit different Li isotopic offsets from seawater ($\Delta^7Li_{fluid\text{-}carb}$), making the original mineralogy a factor when determining seawater δ^7Li values from carbonate archives (fig. 8). The isotope fractionation factor for aragonite is larger than that of calcite (8 to 12‰ *vs*. 1 to 8‰, respectively; Gabitov et al., 2011; Marriott, Henderson, Crompton, et al., 2004; Pogge von Strandmann, Schmidt, et al., 2019). Further, the $\Delta^7Li_{fluid\text{-}carb}$ of biogenic aragonite and calcite is larger than that of inorganic aragonite and calcite, likely due to vital effects (D. Chen et al., 2023), and therefore the relative contributions of biogenic and abiogenic carbonates could also produce variability in bulk carbonate δ^7Li values. As summarized above, $\delta^{44/40}Ca$ values are low and Sr/Ca ratios are high in the Taşkent section (table S1, figs. 3 and 5), both of which characterize aragonite precipitation. Therefore, these data have been interpreted to reflect predominantly aragonitic carbonate sediment and closed-system, or sediment-buffered, conditions (Lau et al., 2017). Although $\delta^{44/40}Ca$ data are not available for the Takachiho or the South China sections, the Sr/Ca ratios from both sections are comparatively lower than those from the Taşkent section (fig. 5). These Sr/Ca differences may indicate that the original proportion of calcite was greater at South China or more extensive recrystallization and alteration during marine, fluid-buffered diagenesis; either hypothesis should be confirmed with additional constraints such as $\delta^{44/40}Ca$ data. Because aragonite has a larger $\Delta^7Li_{fluid\text{-}carb}$ compared to calcite, a difference in $CaCO_3$ mineralogy may also explain lower δ^7Li values in the Taşkent section compared to the South China sections but does not explain why the lowest δ^7Li values occur in the Takachiho section.

One possibility for the notably lower δ^7Li values in the Takachiho section is more extensive diagenetic alteration at this section. Diagenetic alteration, as tracked by Mn/Sr ratio, appears more extensive at Takachiho than at Taşkent (fig. 5). Diagenetic alteration of Takachiho samples may be related to dolomitization; alteration is suggested by an inverse correlation between δ^7Li value and Mg/Ca ratio and a positive correlation between Li/Ca and Mg/Ca ratios (fig. 5). The Mg/Ca ratios of the carbonates from Taşkent are all <100 mmol/mol and only three samples from Shanggang have a Mg/Ca ratio > 100 mmol/mol, whereas the Mg/Ca ratios of the Takachiho carbonates have an average of 230 mmol/mol in the Induan (n=7), with a max of 800 mmol/mol (table S1, fig. 5). Previous work identifying the effect of dolomitization on the δ^7Li value of carbonate minerals has produced mixed results. Experimentally precipitated dolomite suggests a large negative isotope fractionation occurs during dolomite replacement of $CaCO_3$ (Taylor et al., 2019), although the experimental products contain both dolomite and magnesite and therefore a dolomite-specific isotope fractionation factor is not easily calculated. Conversely, direct measurements of dolomitized Neogene carbonates suggest minimal Li isotope fractionation associated with dolomitization, perhaps due to a strongly fluid-buffered diagenetic environment (Dellinger et al., 2020; Liu et al., 2023). Additionally, petrographic evidence for fabric-retentive, early dolomitization from cored car-

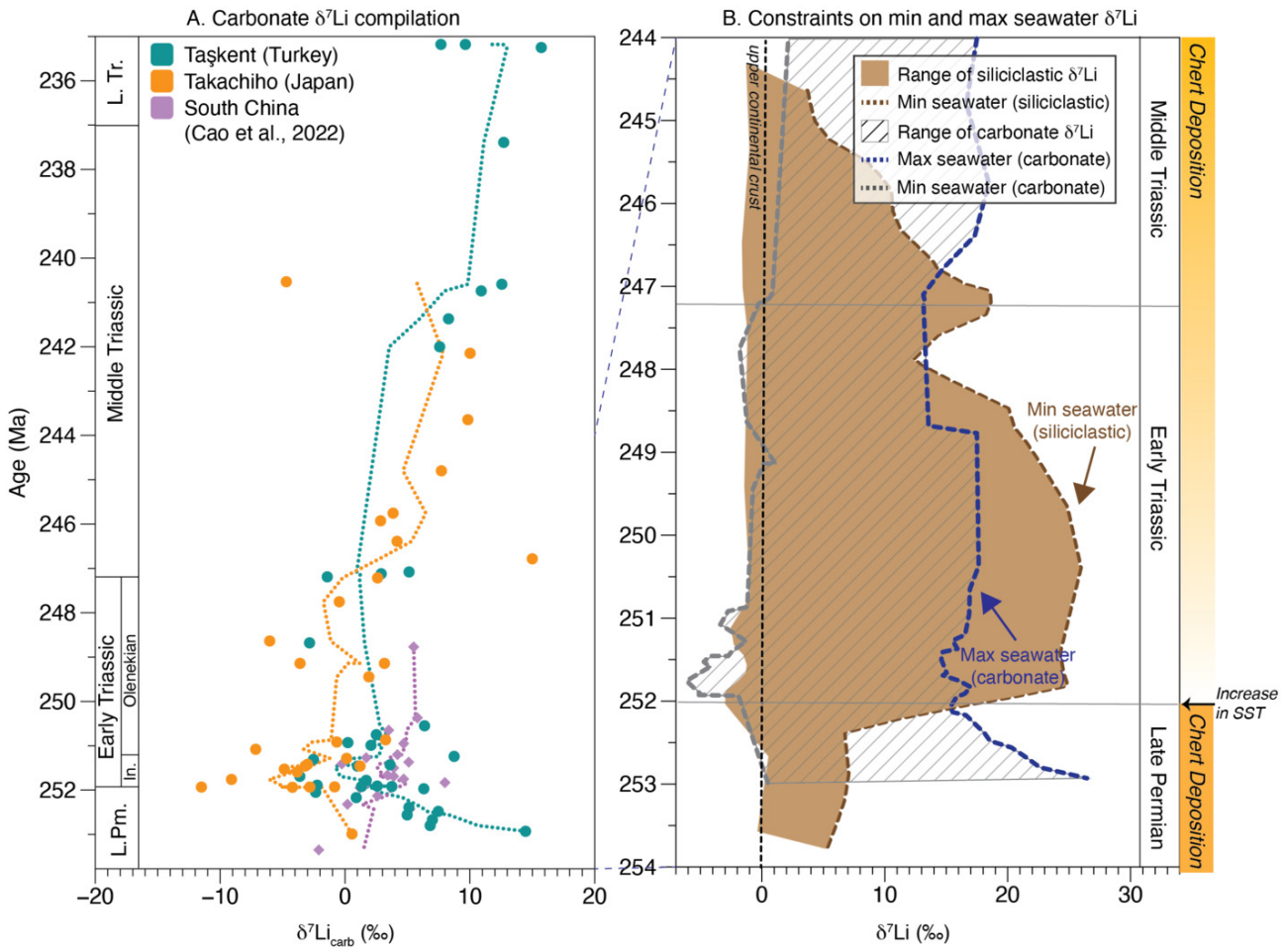

Figure 7. Evolution of carbonate and siliciclastic δ^7Li records. (A) Dotted lines are four-point moving averages for δ^7Li values from carbonate successions that span the latest Permian to the Late Triassic. (B) The range of possible seawater δ^7Li values constrained by Late Permian to Middle Triassic carbonate δ^7Li values is shown in the dashed region. The lower boundary (gray dashed line) represents a Li isotope fractionation factor of 0‰ (i.e., early marine diagenesis), applied to the lowest carbonate δ^7Li values. The upper bound (navy dashed line) represents the largest Li isotope fractionation factor (i.e., aragonite precipitation; $\Delta^7Li_{sw\text{-}carb}$ = 12‰), applied to the highest carbonate δ^7Li values. The brown shaded box indicates the range of siliciclastic δ^7Li records, with the upper bound the lowess fit to the 97.5th percentile of the data from Waiheke, New Zealand and the lower bound constrained by the lowess fit to the 2.5th percentile of the Festningen, Svalbard data (Rauzi et al., 2024). The brown dashed line indicates the minimum seawater δ^7Li value constrained from siliciclastic records. The average upper continental crust δ^7Li value of ~0‰ (Teng et al., 2004) is shown in the vertical dashed line. The increase in sea surface temperatures (SST) occurs at *ca.* 251.84 Ma (Y. Sun et al., 2012). Horizonal dashed lines indicate the time bins discussed in the text. L.Pm. = Late Permian, In. = Induan, L.Tr. = Late Triassic.

bonate sediments from the South China Sea corresponds to a ~0‰ Li isotope fractionation between seawater and dolomite (Liu et al., 2023). The dolomitized samples from Takachiho are from the Lower Triassic and are coarsely recrystallized (L. Zhang et al., 2019). Therefore, later dolomitization at Takachiho may have occurred at higher temperatures more analogous to the experimental dolomites, which could have resulted in Li isotope fractionation different from that observed in Neogene dolomites and produced negative δ^7Li values. It is also possible that fabric-destructive dolomitization at Takachiho was accompanied by diagenesis with a non-seawater fluid that simultaneously increased Mn/Sr ratios.

It is unlikely that spatial or temporal variability in oceanic pH can explain the full range in Triassic δ^7Li values observed among the three sections. An inverse relationship has been observed between $\Delta^7Li_{fluid\text{-}carb}$ and pH for inorganic calcite in several experimental studies (fig. 8; Füger et al., 2022; Gabitov et al., 2011; Marriott, Henderson, Belshaw, et al., 2004; Marriott, Henderson, Crompton, et al., 2004; Seyedali et al., 2021), although another study conducted at higher growth rates displayed the opposite relationship (Day et al., 2021). Assuming the relationship observed for calcite is representative (i.e., larger isotope fractionation with lower pH), fully explaining the ~6 to 10‰ difference in δ^7Li values between the sections in the Induan requires seawater pH at Takachiho to be at least

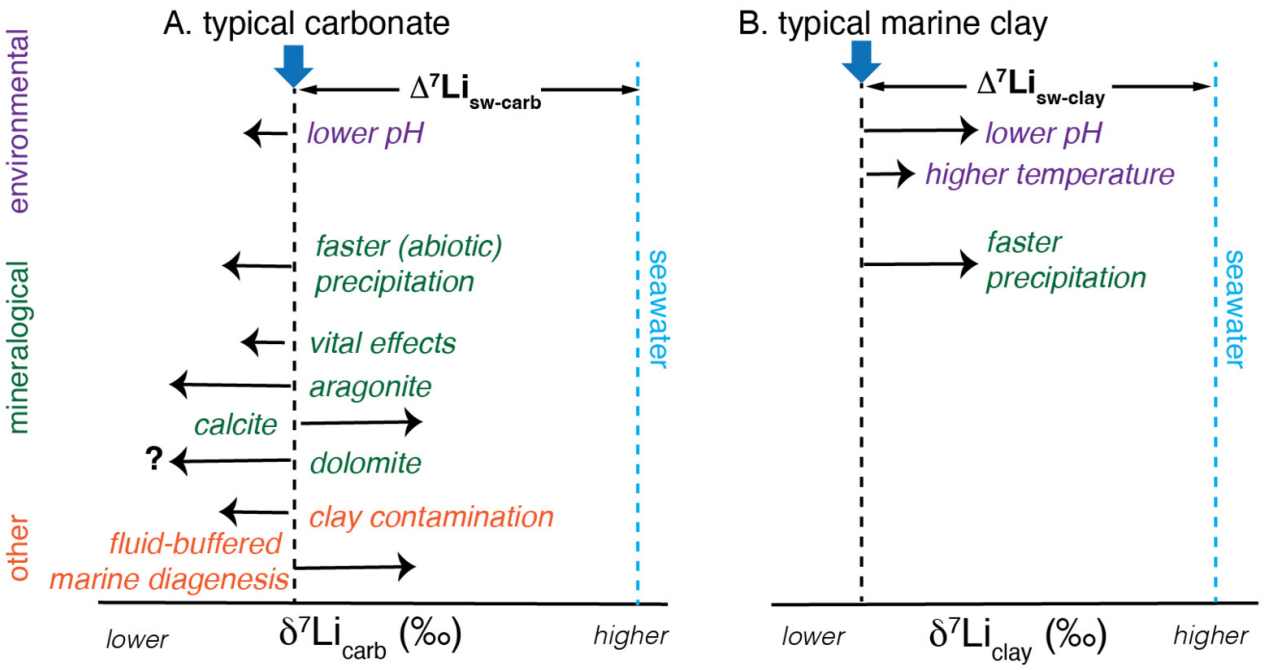

Figure 8. Summary of controls on Li isotope fractionation for (A) carbonates and (B) marine clays. The length of the arrows roughly corresponds to the magnitude of effects on the Li isotope fractionation factor. (A) The Li isotope fractionation of carbonates can vary with pH, abiotic growth rate, vital effects (see D. Chen et al., 2023; F. Li et al., 2021), $CaCO_3$ mineralogy (Gabitov et al., 2011; Marriott, Henderson, Crompton, et al., 2004; Pogge von Strandmann, Schmidt, et al., 2019), clay contamination, and diagenesis. The effects of dolomitization are still unclear (Dellinger et al., 2020; Taylor et al., 2019). (B) The Li isotope fractionation of marine clays can vary with pH, temperature, and reaction rate (Hindshaw et al., 2019). Generally, isotope fractionation for clays is assumed to be larger than for carbonates.

4 pH units more acidic than in the Tethys (D. Chen et al., 2023). Such a large lateral pH gradient is not expected based on modeling that indicates ocean pH varied by less than a pH unit during the Permian–Triassic (Montenegro et al., 2011). There is evidence to indicate that the Early Triassic was characterized by a decrease in marine pH (Black et al., 2014; Clarkson et al., 2015; Knoll et al., 2007; Payne et al., 2010). Using the maximum potential effects from pH and growth rate, up to an 11‰ difference in carbonate δ^7Li values could be explained by a change in environmental factors rather than a change in seawater δ^7Li value or carbonate mineralogy. Higher carbonate δ^7Li values in the Middle Triassic may partially reflect a return to typical ocean pH values and slower carbonate growth rates. However, whether the full stratigraphic shift in Lower Triassic carbonate δ^7Li values was driven by changes in $\Delta^7Li_{sw\text{-}carb}$ is uncertain.

We do not find evidence for siliciclastic contamination as the most parsimonious explanation for the differences in the δ^7Li record among the sections. A few samples from South China have Al/Ca ratios that are higher than at Taşkent and Takachiho, which could indicate siliciclastic contamination (fig. 5), but these samples do not exhibit unusual δ^7Li values. The evidence for siliciclastic contamination is equivocal at Takachiho and unlikely based on its location far from continental siliciclastic sources, and there is no support for contamination in the Taşkent samples, as described above.

Based on these observations, differences in co-eval carbonate δ^7Li values in Turkey, Japan, and South China—and specifically, comparatively low δ^7Li values in Takachiho and comparatively high δ^7Li values in South China—could reflect non-seawater diagenetic alteration associated with dolomitization at Takachiho, and a combination of a higher contribution of aragonite and calcite at Taşkent and South China, respectively. These relative proportions of aragonite and calcite, and the effect of dolomitization as well as marine diagenesis, impacted the Li isotopic offset from seawater in each carbonate section. Low Sr/Ca ratios and high Mn/Sr ratios at South China may indicate more extensive fluid-buffered, early marine diagenesis that increased the carbonate δ^7Li toward higher values. Therefore, reconstructions of seawater δ^7Li values should not be based on a single carbonate section because of the potential for a lithologic control, diagenesis, and clay contamination which can alter the carbonate δ^7Li signal. This conclusion is aligned with a study that compared Permian brachiopod and bulk carbonate δ^7Li value that found that offsets between these components in the same sample varied depending on the site, likely reflecting distinct diagenetic alteration processes (W.-Q. Wang et al., 2024).

4.4. Comparing δ^7Li records in carbonate, siliciclastic, and chert sedimentary archives

Comparing carbonate and siliciclastic Li isotope records has the potential to reveal new insights into the global Li cycle. This approach has been taken for the PETM (Pogge von Strandmann, Jones, et al., 2021), the Hirnantian glaciation (Pogge von Strandmann et al., 2017), and Marinoan glaciation (Yin et al., 2023). In these studies—as in this study—the Li content and isotopic value of marine siliciclastic sediments is assumed to be dictated by the silicate mineral fraction (as opposed to other mineral fractions, such as oxides or carbonates; see discussion in Supplementary Materials), which reflects the combined input of terrestrially derived material (both terrestrially formed clays and unaltered primary minerals) and marine authigenic clays (Chan et al., 2006; Pogge von Strandmann, Dellinger, et al., 2021; Pogge von Strandmann, Fraser, et al., 2019). Terrestrially derived material exhibits a δ^7Li range of −9 to +10‰ reflective of weathering regimes in the modern environment (compiled in Rauzi et al., 2024; e.g., Dellinger et al., 2015, 2017; Huh et al., 1998, 2001; Pogge von Strandmann et al., 2006, 2010; Vigier et al., 2009; C. Yang et al., 2021). Modern marine clays exhibit δ^7Li values above this range (~ +11 to 16‰; Bouman et al., 2004; Chan et al., 2006; G. Li & West, 2014; Lui-Heung & Edmond, 1988; Misra & Froelich, 2012; Vigier et al., 2008). Variation in the δ^7Li values of terrestrially derived material or marine clay, or the relative proportion of terrestrial versus marine clay, can therefore drive changes in siliciclastic sediment δ^7Li values, leading to significant spatial and temporal variability. Given the nature of this simplified two-component mixing system, the δ^7Li value of marine siliciclastic sediment is expected to be spatially variable and dependent on the weathering regime and clay authigenesis of a specific region (i.e., river basin and coastal delta/fan system). In agreement with this framework, a compilation of Lower Triassic marine siliciclastic sediments exhibits a large range in δ^7Li values of nearly 30‰ following the extinction interval (Rauzi et al., 2024). Notably, siliciclastic δ^7Li values in a deep marine section from Southern Panthalassa (modern day New Zealand), containing biogenic chert in a setting far from continental detrital Li inputs, reach values of up to ~27‰ in the Early Triassic, significantly higher than the δ^7Li values of other siliciclastic and carbonate sections from the same interval (fig. 7B; Rauzi et al., 2024). Elevated siliciclastic δ^7Li values in this section, as well as in uppermost Permian and lowermost Triassic shales from Svalbard and Japan (Rauzi et al., 2024), persist in the Early Triassic before returning to pre-perturbation baseline values in the Middle Triassic.

There is no known mechanism that can produce marine authigenic clay δ^7Li values that are higher than that of contemporaneous seawater (fig. 8; see Supplementary Materials for further discussion; Hindshaw et al., 2019). Therefore, the high siliciclastic δ^7Li values observed during the Early Triassic—which are well above the highest suspended sediment δ^7Li values observed in modern rivers—were interpreted to include a marine clay contribution and represent a minimum seawater δ^7Li value during this interval (dashed gray line in fig. 7B; Rauzi et al., 2024). In other words, a shift in the abundance of marine and terrestrial clay over this interval could explain the observed trend. Due to the negative isotope offset associated with Li uptake during marine clay formation, the δ^7Li value of marine clay, or marine siliciclastic sediments that contain authigenic clay, is not directly representative of the seawater δ^7Li value, but instead a minimum constraint. We can apply similar reasoning to the carbonate δ^7Li record for the Early Triassic. The examples of marine diagenesis known to date result in a positive shift from carbonate δ^7Li values below seawater toward, but not exceeding, the δ^7Li value of seawater or the inferred diagenetic fluid (i.e., $\Delta^7Li_{sw\text{-}carb}$ is always < 0‰). If the carbonate δ^7Li values have been only minimally altered, then a large isotope offset from seawater could result. Specifically, if the samples are diagenetically offset with seawater (e.g., $\Delta^7Li_{sw\text{-}carb}$ = 0‰), then a minimum seawater δ^7Li bound can be constrained. Alternatively, if the primary mineralogy was aragonite, pH was relatively low, and diagenetic alteration of the δ^7Li signal is limited, then a $\Delta^7Li_{sw\text{-}carb}$ of 12‰ is possible. We can apply this offset to infer the maximum and minimum seawater δ^7Li signature as determined by the compilation of carbonate δ^7Li values (fig. 7B). Whether these scenarios are likely was discussed in Sections 4.2 and 4.3, but here we take the most conservative approach and apply it broadly across the whole carbonate dataset. We use the minimum δ^7Li value, and assuming complete diagenetic resetting (fig. 7B, dashed gray line), and the maximum δ^7Li value from the carbonate compilation, and assuming the maximum carbonate isotope offset (fig. 7B, dashed navy line), to constrain bounds on the minimum and maximum seawater δ^7Li signatures from the Late Permian to early Middle Triassic.

Comparing the constraints on the seawater δ^7Li signature inferred from these records reveals several surprising observations. First, the maximum seawater δ^7Li values in the Early Triassic, as suggested by the carbonate record, are below the minimum value constrained by the siliciclastic record (fig. 7B). These constraints also imply that $\Delta^7Li_{sw\text{-}carb}$ was at least 20‰ during this time, much larger than the equilibrium isotopic offset determined by experiments and observations of natural carbonate samples in the modern. Finally, these data suggest that the δ^7Li value of authigenic marine clays in the Early Triassic was higher than that of syndepositional carbonates—in other words, a large positive isotopic offset between marine clays and carbonates. This relationship is inverted compared to the modern Li cycle, where the δ^7Li value of marine clay is viewed to be significantly lower than that of carbonate (Chan et al., 2006; Dellinger et al., 2020). The absence of covariance between trends in mean siliciclastic and carbonate δ^7Li value is also in contrast to the PETM and the Hirnantian glaciation, when coeval shale and carbonate δ^7Li records exhibit similar temporal shifts (Pogge von Strandmann et al., 2017; Pogge von Strandmann, Jones, et al., 2021).

The δ^7Li offset between seawater and marine authigenic clays ($\Delta^7Li_{sw\text{-}clay}$ ~20‰ in modern environments; fig. 8) is dependent on temperature (Hindshaw et al., 2019; G. Li &

West, 2014; Vigier et al., 2008), clay formation reaction rate (W. Li & Liu, 2022), mineralogy, and pH (Hindshaw et al., 2019). Elevated seawater temperatures during the Early Triassic (higher by 10 to 15 °C; Joachimski et al., 2020) would explain only a ~2‰ decrease in $\Delta^7Li_{sw\text{-}clay}$ for both marine and terrestrial clay. In addition, an increase in marine dissolved silica concentration driven by the demise of silicifying organisms at the end-Permian is proposed to have resulted in an increase in clay formation reaction rate during the Early Triassic (Isson et al., 2022). This shift could result in a decrease in the $\Delta^7Li_{sw\text{-}clay}$ to values approaching 2‰, which is ~15‰ below the equilibrium value calculated based on temperature for this interval (fig. 1B; Cao et al., 2022; Kalderon-Asael et al., 2021; F. Li et al., 2021). Collectively, environmental changes during the Early Triassic may have driven opposing shifts in $\Delta^7Li_{sw\text{-}carb}$ and $\Delta^7Li_{sw\text{-}clay}$ (fig. 8), resulting in the carbonate δ^7Li value decreasing away from the seawater δ^7Li value and the marine authigenic clay δ^7Li value increasing toward the seawater δ^7Li value. While this framework can explain the deviation in δ^7Li trends observed in either archive, it cannot explain the full difference between carbonates and siliciclastic archives during the Early Triassic. In other words, while the $\Delta^7Li_{sw\text{-}carb}$ may have increased, there is no known mechanism by which it could increase to >20‰, as observed, suggesting that other factors contributed to the trends and inter-archive spread that are observed.

5. CONCEPTUAL MODEL FOR HETEROGENEOUS LI RECORDS AND RECOVERY FROM LI CYCLE PERTURBATIONS FROM THE EARLY TRIASSIC TO THE MIDDLE–LATE TRIASSIC

The carbonate δ^7Li record—from individual sections and aggregated as a whole—consistently supports an increase in carbonate δ^7Li values from ~0‰ (or below for Takachiho) in the Lower Triassic to >0‰ in the Middle Triassic, despite the differences in carbonate sedimentology and diagenetic history. This trend may reflect a global environmental driver on the δ^7Li cycle. The decrease in carbonate δ^7Li values in the latest Permian has been explained by an increase in reverse weathering, and a decrease in associated isotope fractionation, in the latest Permian that decreased and sustained low seawater δ^7Li values in the Early Triassic (Cao et al., 2022; Isson et al., 2022; Rauzi et al., 2024). The new carbonate δ^7Li records presented in this study extend the previous compilation (fig. 7A), indicating that carbonate δ^7Li values increased steadily from the Middle to the Late Triassic to ~15‰, comparable to carbonate δ^7Li values observed earlier in the Permian (Cao et al., 2022). The sustained low carbonate δ^7Li values in the Early Triassic could also be interpreted to reflect a higher silicate weathering flux of Li, associated with climate changes from Siberian Traps degassing (fig. 9). Therefore, if the carbonate δ^7Li trends can be interpreted to reflect changes in the seawater δ^7Li signature, they would imply a decrease in continental silicate weathering and reverse weathering Li fluxes that accompanied the return to cooler sea surface temperatures and lower atmospheric pCO_2 in the Middle Triassic (fig. 9; Joachimski et al., 2022; Y. Sun et al., 2012). Both responses are expected if climate recovery resulted in less intense continental weathering and if the return of silica biomineralizers reduced dissolved silica concentrations and therefore, reverse weathering rates. These interpretations are consistent with seawater Li isotope modeling for the Late Permian to the Early Triassic (Cao et al., 2022; Rauzi et al., 2024). However, as discussed in Sections 4.2 and 4.3, diagenetic alteration can result in stratigraphic variations in carbonate δ^7Li records over time. This makes the interpreted Li cycle changes from the Early to Middle/Late Triassic speculative, though future constraints from $\delta^{44/40}Ca$ records from the same sections as those with δ^7Li data will be invaluable for assessing our current interpretations.

Nonetheless, even after accounting for carbonate diagenetic effects, the very low carbonate δ^7Li values in the Early Triassic and the notable differences among carbonate and siliciclastic δ^7Li records complicate a simple explanation of global Li isotope cycle perturbations and indicate a Li cycle distinct from the modern (fig. 9). Specifically, constraints on the seawater δ^7Li signature conflict, with minimum seawater δ^7Li estimates from siliciclastic records exhibiting higher values than the maximum seawater δ^7Li estimates from carbonate records (fig. 7B). We speculate that the discrepancies among Lower Triassic carbonate and siliciclastic δ^7Li records may be a symptom of a highly perturbed Li cycle in the Early Triassic. Here, we consider the possibility that both archives record their local source fluid, and that the δ^7Li value was heterogeneous laterally and with depth in the ocean during this interval. Carbon cycle modeling suggests an increase in silicate weathering flux by two- to three-fold (Isson et al., 2022). Terrestrial weathering congruency is expected to increase due to more active hydrologic cycle and higher temperatures, which would decrease riverine δ^7Li values (Dellinger et al., 2015; F. Zhang et al., 2022). Together, these changes in continental weathering could result in a two- to three-fold increase in the dissolved riverine flux of Li to the marine environment (Rauzi et al., 2024) and a decrease in the δ^7Li value of the dissolved riverine input (due to a reduction in secondary clay formation) to crustal-like δ^7Li values (Dellinger et al., 2015; Huh et al., 1998; Misra & Froelich, 2012; Pogge von Strandmann et al., 2013; Rugenstein et al., 2019; F. Zhang et al., 2022). However, an even greater coeval increase in Li uptake into marine authigenic clays (Isson et al., 2022; Rauzi et al., 2024) could have driven an overall depletion in the global marine Li reservoir and reduced the residence time of Li in the ocean in the Early Triassic. The potential for reverse weathering to significantly impact the Li cycle remains speculative given the uncertainty around the extent and contribution of reverse weathering even in the modern oceans; further work is needed to confirm this in modern settings.

A reduced marine Li reservoir and shorter residence time potentially resulted in a poorly mixed Li reservoir (fig. 9). The return of silica biomineralizers in the Middle Triassic would have reduced marine authigenic clay formation and

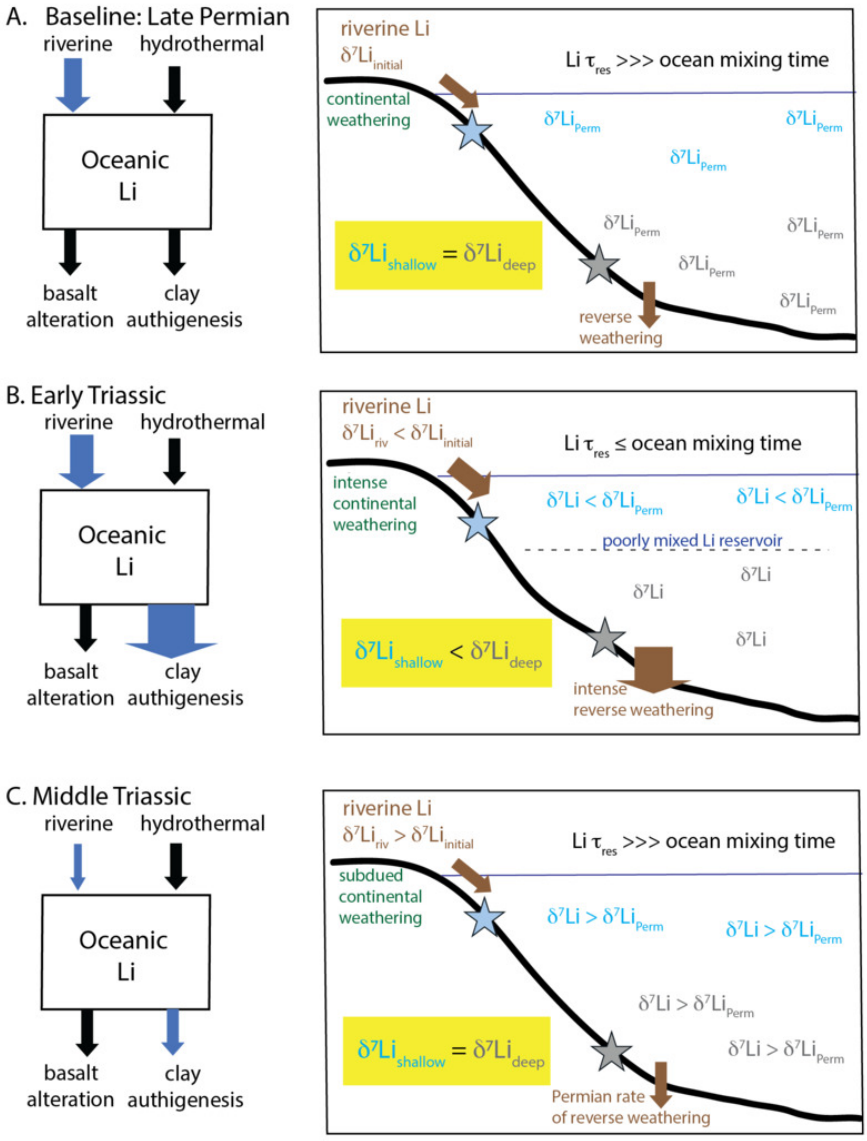

Figure. 9. Schematic of possible changes to the global Li cycle from the Late Permian to the Middle Triassic. Fluxes noted with blue arrows in mass balance cartoons are interpreted to have changed over this interval. In the Late Permian, the oceanic Li reservoir is large and δ^7Li value is conservative. A ~50 Myr carbonate δ^7Li record suggests weathering in the Late Permian was highly congruent compared to the Early Permian (Cao et al., 2022). A large Li reservoir resulted in no difference in δ^7Li value between the shallow and deep ocean, which are recorded in carbonates (blue star; this study and Cao et al., 2022) and siliciclastics (gray star; Rauzi et al., 2024), respectively. In the Early Triassic, continental and reverse weathering both intensified, potentially leading to a net decrease in the oceanic Li reservoir. If the Li reservoir decreased such that Li was no longer conservative (i.e., a substantial decrease in the residence time), seawater δ^7Li values may have been heterogeneous. In this scenario, δ^7Li value in the shallow ocean may have been very low due to intensified continental weathering, resulting in lower δ^7Li values in shallow marine carbonates (blue star). In contrast, δ^7Li values in the deep ocean could have reflected changes in inputs as well as more intense clay authigenesis, resulting in higher δ^7Li values in basinal siliciclastic sediments (gray star). In the Middle Triassic, the Li cycle recovered and returned to conservative behavior. Higher δ^7Li values in Middle Triassic carbonates (this study) suggest both the weathering and reverse weathering fluxes of Li were lower than in the Late Permian and Early Triassic.

returned the marine Li reservoir to pre-extinction, well-mixed conditions with a homogenous seawater δ^7Li value. Until that point, a depth gradient in δ^7Li values could develop if the shallow-water Li pool was dominated by continental sources. This shallow, coastally dominated seawater may have been characterized by low δ^7Li values reflecting riverine geochemistry and local depositional conditions (e.g., precipitation rate, pH). Modeling of the global δ^7Li cycle (Cao et al., 2022; Rauzi et al., 2024) suggests that the δ^7Li value of rivers could have been as low as 7‰ in

the Early Triassic, implying that $\Delta^7Li_{sw\text{-}carb}$ was at ~10‰, within the range of values observed for aragonite (e.g., Marriott, Henderson, Crompton, et al., 2004). More distal siliciclastic sections may have recorded a deep marine δ^7Li value that was strongly modulated by authigenic clay precipitation on the seafloor rather than direct continental inputs. By the Middle Triassic, the δ^7Li values of siliciclastic sediments return to values lower than coeval carbonates (i.e., negative $\Delta^7Li_{clay\text{-}carb}$), akin to the modern δ^7Li cycle (figs. 7B, 9C).

Although the Takachiho section represents an isolated atoll in the middle of the Panthalassa Ocean, far from continental sources, it is possible that oceanographic patterns could have transported riverine Li from Pangaea to this site. With the cGENIE Earth system model of intermediate complexity (see Supplementary Materials for details), we use a conservative tracer to illustrate a mechanism by which it could be possible for riverine Li—in a highly altered Li cycle—to influence the δ^7Li value in the paleogeographic setting of Takachiho (fig. 10). A conservative tracer approach is not intended to be a perfect analog for the behavior of Li in the marine environment (i.e., there is no representation of Li removal from the ocean, nor does it capture Li reactions on the shallow shelves). However, this treatment of riverine Li as a conservative input to seawater Li is a common approach in other studies (e.g., mass balance model in Cao et al., 2022). This approach is also supported by studies of Li isotope mixing at the Changjiang River estuary (C. Yang et al., 2021). This study observed modification of riverine dissolved δ^7Li value was limited during estuarine processes and therefore could retain its signature before being mixed with seawater (C. Yang et al., 2021). Where mixing with seawater occurs, and the timescale on which it happens, depends on the open ocean Li reservoir size.

The model results indicate how the surface seawater Li inventory in the mid-Panthalassa can potentially be influenced by riverine Li sources via circulation in an ocean characterized by a small Li reservoir. In all cases, the tracer is transported to the location of Takachiho (fig. 10). Scenario (A) is likely to be most representative of weathering fluxes at the western margin of equatorial Pangea due to higher runoff inferred for this paleogeography (Scotese, 2014). Coastal precipitation, and by extension runoff, is simulated to be highest at the equator along the western margin of Pangea (X. Li et al., 2022; Scotese, 2014). Based on these results, we hypothesize that the lateral spatial variability in carbonate δ^7Li values reflects differences in the Li isotope fractionation during carbonate precipitation and from diagenetic alteration, the degree of mixing between riverine and deep-ocean Li reservoirs with differing δ^7Li values, and potentially, differences in the riverine δ^7Li values that reflect regional weathering dynamics.

It is currently difficult to evaluate the possibility of heterogeneous seawater δ^7Li values, and whether a poorly mixed seawater Li reservoir is feasible on these timescales. Large changes in the marine Li reservoir, sustained on 10^6 yr timescales, have been proposed, with a nearly 7-fold decrease in seawater Li concentrations reconstructed in the

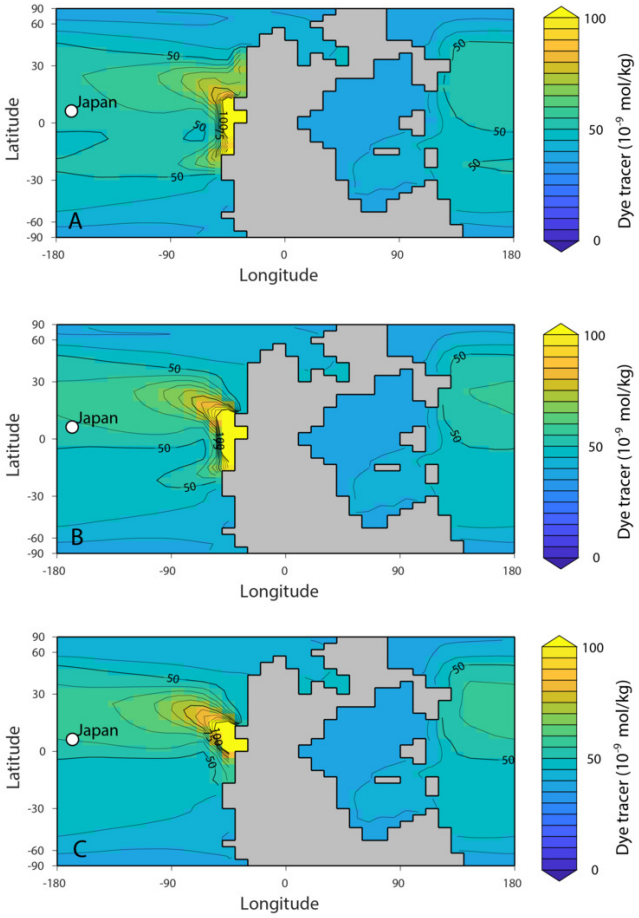

Figure 10. Sensitivity tests of transport of a conservative dye tracer in the Panthalassic Ocean to the Takachiho, Japan site as a proxy for potential transport of continental Li with low δ^7Li values. A global input flux of 2 x 10^{10} mol/yr, approximately the flux of riverine Li estimated for the Early Triassic (Rauzi et al., 2024) is added to the oceans along the western margin of Pangea (A) across the entire west coast, with a 2x rate in the tropics (~13°N to ~13°S); (B) only in the tropics; and (C) as a point source at the equator.

Jurassic compared to today (G. Li & West, 2014; Rugenstein et al., 2019; Weldeghebriel & Lowenstein, 2023). A model of the Early Triassic Li cycle (Rauzi et al., 2024) calculated a minimum Li residence time of 78 kyr. The model was designed such that seawater Li concentrations were not allowed to decrease below 10% of levels in today's oceans; therefore, a true minimum residence time was not calculated and could conceivably be lower. Thus, it is reasonable to hypothesize that a substantial change in the Li fluxes would have similarly reduced the residence time in the Early Triassic, and future work with Li models could provide quantitative constraints on this change (e.g., Adloff et al., 2021). If seawater Li had a residence time of 78 kyr or lower, it would be possible for spatial heterogeneity to occur. For example, seawater dissolved inorganic carbon (DIC) is estimated to have a residence time of 83 to 200 kyr today (Berner & Berner, 1997; Zeebe & Wolf-Gladrow, 2009), and

vertical and lateral DIC profiles are observed today due to uptake via primary productivity and release from remineralization. Though the Li and DIC cycles are not controlled by the same processes, this comparison demonstrates that geochemical cycles with residence times on the order of 10^5 yr have the potential to be poorly mixed in the ocean. Nonetheless, the potential recovery of Li cycling in the Middle to Late Triassic would increase the Li residence time, returning seawater Li to being a conservative element as is observed today.

6. CONCLUSION

We present carbonate δ^7Li records from shallow marine sections in the western Tethys (Taşkent, Turkey) and an isolated atoll in the Panthalassic Ocean (Takachiho, Japan) that span the uppermost Permian to the Late Triassic. These sections provide the first carbonate δ^7Li record that covers the entire recovery period from the end-Permian mass extinction. Following low δ^7Li values in Lower Triassic carbonates, our new data record a shift in the Middle Triassic to higher values similar to those of the Middle Permian and early Late Permian. Carbonate δ^7Li values are low in the Induan (lowermost Triassic), with values near 0‰ that potentially reflect decreased ocean pH and elevated mineral growth rates that could have increased the Li isotopic offset from the precipitating fluid. During this interval, values differ by up to ~20‰ between the study sections and published carbonate records, which we attribute to variable diagenetic alteration, potentially related to later dolomitization, as well as different proportions of aragonite and calcite. Even after accounting for diagenetic alteration, carbonate δ^7Li values in the Early Triassic are inconsistent with seawater δ^7Li estimates from siliciclastic records of the same interval (Rauzi et al., 2024). An assessment of Li cycle archives from the Early Triassic supports *(1)* an increase in congruent continental silicate weathering that increased the Li flux and decreased the δ^7Li value of the dissolved riverine Li input to the ocean and *(2)* a coeval elevated rate of reverse weathering (driven by the decimation of silica biomineralizers) that increased the marine Li removal flux. We propose that these inconsistencies reflect a marine Li cycle that was out of equilibrium in the Early Triassic, characterized by a short oceanic Li residence time and a spatial heterogeneity in seawater δ^7Li values. As a result, a Lower Triassic carbonate δ^7Li value may not be directly recording perturbations to the global Li cycle. Instead, it could track the δ^7Li value of shallow waters more strongly impacted by continental Li sources. In the Middle Triassic, the return of silica biomineralizers is predicted to result in lower reverse weathering rates (Isson et al., 2022), returning the seawater Li cycle to more typical conditions.

Data Availability Statement

All analytical data are provided in the supplemental table.
https://doi.org/10.26207/xah3-3r67

Acknowledgments

This research was supported by a Sloan Foundation Fellowship to K.V.L., a NASA PA Space Grant award to K.V.L. and K.T., and a National Science Foundation Continental Dynamics Grant EAR-0807475 to J.L.P. D.H. was supported by a postdoctoral fellowship from the Cluster of Excellence "The Ocean Floor–Earth's Uncharted Interface" (research unit recorder), DFG 390741603. The data presented in this study were partially produced by the Laboratory for Isotopes and Metals in the Environment (LIME) at the Pennsylvania State University. We are grateful for analytical assistance from Dan Asael (Yale), Dave Mucciarone (Stanford), and Maggie Wang and Laura Liermann (LIME, Penn State). T.I. acknowledges support from the Marsden Fund (MFP-UOW2010) and the Rutherford Discovery Fellowship (Royal Society of New Zealand, RDF-UOW-2201). We sincerely appreciate the valuable comments and suggestions from one anonymous reviewer, Michael Kipp, and the associate editor, which have significantly improved the quality of this manuscript.

Author Contributions

Kaitlin Taylor: Investigation, Writing – original draft. Sofia Rauzi: Validation, Writing – Reviewing and Editing. Terry Isson: Validation, Writing – Reviewing and Editing. Daniel Ibarra: Investigation, Writing – review and editing. Dominik Huĭse: Software, Formal Analysis, Writing – review and editing. Sara Kimmig: Investigation, Methodology, Writing – review and editing. Jonathan Payne: Conceptualization, Resources, Formal Analysis, Writing – review and editing. Demir Altiner: Resources, Writing – review and editing. Daniel Lehrmann: Resources, Writing – review and editing. Boriana Asael-Kalderon: Investigation, Methodology. Noah Planavsky: Conceptualization. Kimberly Lau – Conceptualization, Supervision, Formal Analysis, Visualization, Validation, Writing – review and editing.

Conflicts of Interest

The authors declare no conflict of interest.

Editor: Francis Macdonald, Associate Editor: A. Joshua West

Submitted: June 04, 2025 EDT. Accepted: February 01, 2026 EDT. Published: March 23, 2026 EDT.

REFERENCES

Adloff, M., Ridgwell, A., Monteiro, F. M., Parkinson, I. J., Dickson, A. J., Pogge von Strandmann, P. A. E., Fantle, M. S., & Greene, S. E. (2021). Inclusion of a suite of weathering tracers in the cGENIE Earth system model – muffin release v.0.9.23. *Geoscientific Model Development*, *14*(7), 4187–4223. https://doi.org/10.5194/gmd-14-4187-2021

Altıner, D., & Özgül, N. (2001). Carboniferous and Permian of the allochtonous terranes of the Central Tauride Belt, southern Turkey. In *PaleoForams 2001, International Conference of Paleozoic Benthic Foraminifera (Ankara), Guidebook*.

Altıner, D., Payne, J. L., Lehrmann, D. J., Atasoy, S. G., & Özkan-Altıner, S. (2024). New foraminifera from the Changhsingian (Upper Permian) of the Taurides (southern Turkey) with remarks on their evolutionary origins. *Journal of Paleontology*, *98*(5), 745–772. https://doi.org/10.1017/jpa.2024.21

Altıner, D., Payne, J. L., Lehrmann, D. J., Özkan-Altıner, S., Kelley, B. M., Summers, M. M., & Yu, M. (2021). Triassic Foraminifera from the Great Bank of Guizhou, Nanpanjiang Basin, south China: Taxonomic account, biostratigraphy, and implications for recovery from end-Permian mass extinction. *Journal of Paleontology*, *95*(S84), 1–53. https://doi.org/10.1017/jpa.2021.10

Baud, A., Cirilli, S., & Marcoux, J. (1997). Biotic Response to Mass Extinction: The lowermost Triassic Microbialites. *Facies*, *36*, 238–242.

Baud, A., Richoz, S., & Marcoux, J. (2005). Calcimicrobial cap rocks from the basal Triassic units: Western Taurus occurrences (SW Turkey). *Comptes Rendus Palevol*, *4*(6–7), 569–582. https://doi.org/10.1016/j.crpv.2005.03.001

Beauchamp, B., & Baud, A. (2002). Growth and demise of Permian biogenic chert along northwest Pangea: Evidence for end-Permian collapse of thermohaline circulation. *Palaeogeography, Palaeoclimatology, Palaeoecology*, *184*(1–2), 37–63. https://doi.org/10.1016/S0031-0182(02)00245-6

Berner, R. A., & Berner, E. K. (1997). Silicate Weathering and Climate. In *Tectonic Uplift and Climate Change* (pp. 353–365). https://doi.org/10.1007/978-1-4615-5935-1_15

Black, B. A., Lamarque, J.-F., Shields, C. A., Elkins-Tanton, L. T., & Kiehl, J. T. (2014). Acid rain and ozone depletion from pulsed Siberian Traps magmatism. *Geology*, *42*(1), 67–70. https://doi.org/10.1130/G34875.1

Bouman, C., Elliott, T., & Vroon, P. Z. (2004). Lithium inputs to subduction zones. *Chemical Geology*, *212*(1–2), 59–79. https://doi.org/10.1016/j.chemgeo.2004.08.004

Burgess, S. D., Bowring, S., & Shen, S.-Z. (2014). High-precision timeline for Earth's most severe extinction. *Proceedings of the National Academy of Sciences*, *111*(9), 3316–3321. https://doi.org/10.1073/pnas.1317692111

Burton, K. W., & Vigier, N. (2012). Lithium Isotopes as Tracers in Marine and Terrestrial Environments. In M. Baskaran (Ed.), *Handbook of Environmental Isotope Geochemistry: Vol I* (pp. 41–59). Springer Berlin Heidelberg. https://doi.org/10.1007/978-3-642-10637-8_4

Cao, C., Bataille, C. P., Song, H., Saltzman, M. R., Tierney Cramer, K., Wu, H., Korte, C., Zhang, Z., & Liu, X.-M. (2022). Persistent late Permian to Early Triassic warmth linked to enhanced reverse weathering. *Nature Geoscience*, *15*(10), 832–838. https://doi.org/10.1038/s41561-022-01009-x

Cao, C., Liu, X.-M., Wang, X.-K., & Chen, J. (2023). Effective use of limestones to reconstruct seawater Li isotope compositions - A community standard proposal. *Chemical Geology*, *626*, 121441. https://doi.org/10.1016/j.chemgeo.2023.121441

Chan, L.-H., Leeman, W. P., & Plank, T. (2006). Lithium isotopic composition of marine sediments. *Geochemistry, Geophysics, Geosystems*, *7*(6), 2005GC001202. https://doi.org/10.1029/2005GC001202

Chen, D., Thibon, F., Felbacq, A., Weppe, L., Metian, M., & Vigier, N. (2023). Coupled survey of lithium isotopes and Li/Ca in biogenic and inorganic carbonates. *Earth-Science Reviews*, *244*, 104500. https://doi.org/10.1016/j.earscirev.2023.104500

Chen, Z.-Q., & Benton, M. J. (2012). The timing and pattern of biotic recovery following the end-Permian mass extinction. *Nature Geoscience*, *5*(6), 375–383. https://doi.org/10.1038/ngeo1475

Clarkson, M. O., Kasemann, S. A., Wood, R. A., Lenton, T. M., Daines, S. J., Richoz, S., Ohnemueller, F., Meixner, A., Poulton, S. W., & Tipper, E. T. (2015). Ocean acidification and the Permo-Triassic mass extinction. *Science*, *348*(6231), 229–232. https://doi.org/10.1126/science.aaa0193

Coogan, L. A., Gillis, K. M., Pope, M., & Spence, J. (2017). The role of low-temperature (off-axis) alteration of the oceanic crust in the global Li-cycle: Insights from the Troodos ophiolite. *Geochimica et Cosmochimica Acta*, *203*, 201–215. https://doi.org/10.1016/j.gca.2017.01.002

Crockford, P. W., Kunzmann, M., Blättler, C. L., Kalderon-Asael, B., Murphy, J. G., Ahm, A.-S., Sharoni, S., Halverson, G. P., Planavsky, N. J., Halevy, I., & Higgins, J. A. (2021). Reconstructing Neoproterozoic seawater chemistry from early diagenetic dolomite. *Geology*, *49*(4), 442–446. https://doi.org/10.1130/G48213.1

Day, C. C., Pogge von Strandmann, P. A. E., & Mason, A. J. (2021). Lithium isotopes and partition coefficients in inorganic carbonates: Proxy calibration for weathering reconstruction. *Geochimica et Cosmochimica Acta*, *305*, 243–262. https://doi.org/10.1016/j.gca.2021.02.037

Dellinger, M., Bouchez, J., Gaillardet, J., Faure, L., & Moureau, J. (2017). Tracing weathering regimes using the lithium isotope composition of detrital sediments. *Geology*, *45*(5), 411–414. https://doi.org/10.1130/G38671.1

Dellinger, M., Gaillardet, J., Bouchez, J., Calmels, D., Louvat, P., Dosseto, A., Gorge, C., Alanoca, L., & Maurice, L. (2015). Riverine Li isotope fractionation in the Amazon River basin controlled by the weathering regimes. *Geochimica et Cosmochimica Acta*, *164*, 71–93. https://doi.org/10.1016/j.gca.2015.04.042

Dellinger, M., Hardisty, D. S., Planavsky, N. J., Gill, B. C., Kalderon-Asael, B., Asael, D., Croissant, T., Swart, P. K., & West, A. J. (2020). The effects of diagenesis on lithium isotope ratios of shallow marine carbonates. *American Journal of Science*, *320*(2), 150–184. https://doi.org/10.2475/02.2020.03

Dellinger, M., West, A. J., Paris, G., Adkins, J. F., Pogge von Strandmann, P. A. E., Ullmann, C. V., Eagle, R. A., Freitas, P., Bagard, M.-L., Ries, J. B., Corsetti, F. A., Perez-Huerta, A., & Kampf, A. R. (2018). The Li isotope composition of marine biogenic carbonates: Patterns and mechanisms. *Geochimica et Cosmochimica Acta*, *236*, 315–335. https://doi.org/10.1016/j.gca.2018.03.014

Fantle, M. S., Barnes, B. D., & Lau, K. V. (2020). The Role of Diagenesis in Shaping the Geochemistry of the Marine Carbonate Record. *Annual Review of Earth and Planetary Sciences*, *48*(1), 549–583. https://doi.org/10.1146/annurev-earth-073019-060021

Fantle, M. S., & DePaolo, D. J. (2007). Ca isotopes in carbonate sediment and pore fluid from ODP Site 807A: The Ca^{2+}(aq)–calcite equilibrium fractionation factor and calcite recrystallization rates in Pleistocene sediments. *Geochimica et Cosmochimica Acta*, *71*(10), 2524–2546. https://doi.org/10.1016/j.gca.2007.03.006

Fantle, M. S., & Higgins, J. (2014). The effects of diagenesis and dolomitization on Ca and Mg isotopes in marine platform carbonates: Implications for the geochemical cycles of Ca and Mg. *Geochimica et Cosmochimica Acta*, *142*, 458–481. https://doi.org/10.1016/j.gca.2014.07.025

Füger, A., Kuessner, M., Rollion-Bard, C., Leis, A., Magna, T., Dietzel, M., & Mavromatis, V. (2022). Effect of growth rate and pH on Li isotope fractionation during its incorporation in calcite. *Geochimica et Cosmochimica Acta*, *323*, 276–290. https://doi.org/10.1016/j.gca.2022.02.014

Gabitov, R. I., Schmitt, A. K., Rosner, M., McKeegan, K. D., Gaetani, G. A., Cohen, A. L., Watson, E. B., & Harrison, T. M. (2011). In situ δ^7Li, Li/Ca, and Mg/Ca analyses of synthetic aragonites. *Geochemistry, Geophysics, Geosystems*, *12*(3). https://doi.org/10.1029/2010GC003322

Groves, J. R., Altiner, D., & Rettori, R. (2005). EXTINCTION, SURVIVAL, AND RECOVERY OF LAGENIDE FORAMINIFERS IN THE PERMIAN–TRIASSIC BOUNDARY INTERVAL, CENTRAL TAURIDES, TURKEY. *Journal of Paleontology*, *79*(sp62), 1–38. https://doi.org/10.1666/0022-3360(2005)79[1:esarol]2.0.co;2

Gussone, N., Ahm, A.-S. C., Lau, K. V., & Bradbury, H. J. (2020). Calcium isotopes in deep time: Potential and limitations. *Chemical Geology*, *544*, 119601. https://doi.org/10.1016/j.chemgeo.2020.119601

Hallam, A. (1991). Why was there a delayed radiation after the end-Palaeozoic extinctions? *Historical Biology*, *5*(2–4), 257–262. https://doi.org/10.1080/10292389109380405

Hathorne, E., & James, R. (2006). Temporal record of lithium in seawater: A tracer for silicate weathering? *Earth and Planetary Science Letters*, *246*(3–4), 393–406. https://doi.org/10.1016/j.epsl.2006.04.020

Hindshaw, R. S., Tosca, R., Goût, T. L., Farnan, I., Tosca, N. J., & Tipper, E. T. (2019). Experimental constraints on Li isotope fractionation during clay formation. *Geochimica et Cosmochimica Acta*, *250*, 219–237. https://doi.org/10.1016/j.gca.2019.02.015

Hinojosa, J. L., Brown, S. T., Chen, J., DePaolo, D. J., Paytan, A., Shen, S. -z., & Payne, J. L. (2012). Evidence for end-Permian ocean acidification from calcium isotopes in biogenic apatite. *Geology*, *40*(8), 743–746. https://doi.org/10.1130/G33048.1

Horacek, M., Koike, T., & Richoz, S. (2009). Lower Triassic $\delta^{13}C$ isotope curve from shallow-marine carbonates in Japan, Panthalassa realm: Confirmation of the Tethys $\delta^{13}C$ curve. *Journal of Asian Earth Sciences*, *36*(6), 481–490. https://doi.org/10.1016/j.jseaes.2008.05.005

Huang, K.-F., You, C.-F., Liu, Y.-H., Wang, R.-M., Lin, P.-Y., & Chung, C.-H. (2010). Low-memory, small sample size, accurate and high-precision determinations of lithium isotopic ratios in natural materials by MC-ICP-MS. *Journal of Analytical Atomic Spectrometry*, *25*(7), 1019. https://doi.org/10.1039/b926327f

Huh, Y., Chan, L.-H., & Edmond, J. M. (2001). Lithium isotopes as a probe of weathering processes: Orinoco River. *Earth and Planetary Science Letters*, *194*(1–2), 189–199. https://doi.org/10.1016/S0012-821X(01)00523-4

Huh, Y., Chan, L.-H., Zhang, L., & Edmond, J. M. (1998). Lithium and its isotopes in major world rivers: Implications for weathering and the oceanic budget. *Geochimica et Cosmochimica Acta*, *62*(12), 2039–2051. https://doi.org/10.1016/S0016-7037(98)00126-4

Isson, T. T., & Planavsky, N. J. (2018). Reverse weathering as a long-term stabilizer of marine pH and planetary climate. *Nature*, *560*(7719), 471–475. https://doi.org/10.1038/s41586-018-0408-4

Isson, T. T., Planavsky, N. J., Coogan, L. A., Stewart, E. M., Ague, J. J., Bolton, E. W., Zhang, S., McKenzie, N. R., & Kump, L. R. (2020). Evolution of the Global Carbon Cycle and Climate Regulation on Earth. *Global Biogeochemical Cycles*, *34*(2), e2018GB006061. https://doi.org/10.1029/2018GB006061

Isson, T. T., & Rauzi, S. (2024). Oxygen isotope ensemble reveals Earth's seawater, temperature, and carbon cycle history. *Science*, *383*(6683), 666–670. https://doi.org/10.1126/science.adg1366

Isson, T. T., Zhang, S., Lau, K. V., Rauzi, S., Tosca, N. J., Penman, D. E., & Planavsky, N. J. (2022). Marine siliceous ecosystem decline led to sustained anomalous Early Triassic warmth. *Nature Communications*, *13*(1), 3509. https://doi.org/10.1038/s41467-022-31128-3

Joachimski, M. M., Alekseev, A. S., Grigoryan, A., & Gatovsky, Y. A. (2020). Siberian Trap volcanism, global warming and the Permian-Triassic mass extinction: New insights from Armenian Permian-Triassic sections. *Geological Society of America Bulletin*, *132*(1–2), 427–443. https://doi.org/10.1130/B35108.1

Joachimski, M. M., Müller, J., Gallagher, T. M., Mathes, G., Chu, D. L., Mouraviev, F., Silantiev, V., Sun, Y. D., & Tong, J. N. (2022). Five million years of high atmospheric CO_2 in the aftermath of the Permian-Triassic mass extinction. *Geology*, *50*(6), 650–654. https://doi.org/10.1130/G49714.1

Kalderon-Asael, B., Katchinoff, J. A. R., Planavsky, N. J., Hood, A. v. S., Dellinger, M., Bellefroid, E. J., Jones, D. S., Hofmann, A., Ossa, F. O., Macdonald, F. A., Wang, C., Isson, T. T., Murphy, J. G., Higgins, J. A., West, A. J., Wallace, M. W., Asael, D., & Pogge von Strandmann, P. A. E. (2021). A lithium-isotope perspective on the evolution of carbon and silicon cycles. *Nature*, *595*(7867), 394–398. https://doi.org/10.1038/s41586-021-03612-1

Knoll, A. H., Bambach, R. K., Payne, J. L., Pruss, S., & Fischer, W. W. (2007). Paleophysiology and end-Permian mass extinction. *Earth and Planetary Science Letters*, *256*(3–4), 295–313. https://doi.org/10.1016/j.epsl.2007.02.018

Komar, N., & Zeebe, R. E. (2016). Calcium and calcium isotope changes during carbon cycle perturbations at the end-Permian. *Paleoceanography*, *31*(1), 115–130. https://doi.org/10.1002/2015PA002834

Korte, C., Kozur, H. W., Bruckschen, P., & Veizer, J. (2003). Strontium isotope evolution of Late Permian and Triassic seawater. *Geochimica et Cosmochimica Acta*, *67*(1), 47–62. https://doi.org/10.1016/S0016-7037(02)01035-9

Krause, A. J., Sluijs, A., van der Ploeg, R., Lenton, T. M., & Pogge von Strandmann, P. A. E. (2023). Enhanced clay formation key in sustaining the Middle Eocene Climatic Optimum. *Nature Geoscience*, *16*(8), 730–738. https://doi.org/10.1038/s41561-023-01234-y

Kump, L. R. (2018). Prolonged Late Permian–Early Triassic hyperthermal: Failure of climate regulation? *Philosophical Transactions of the Royal Society A: Mathematical, Physical and Engineering Sciences*, *376*(2130), 20170078. https://doi.org/10.1098/rsta.2017.0078

Lau, K. V., Maher, K., Altiner, D., Kelley, B. M., Kump, L. R., Lehrmann, D. J., Silva-Tamayo, J. C., Weaver, K. L., Yu, M., & Payne, J. L. (2016). Marine anoxia and delayed Earth system recovery after the end-Permian extinction. *Proceedings of the National Academy of Sciences*, *113*(9), 2360–2365. https://doi.org/10.1073/pnas.1515080113

Lau, K. V., Maher, K., Brown, S. T., Jost, A. B., Altıner, D., DePaolo, D. J., Eisenhauer, A., Kelley, B. M., Lehrmann, D. J., Paytan, A., Yu, M., Silva-Tamayo, J. C., & Payne, J. L. (2017). The influence of seawater carbonate chemistry, mineralogy, and diagenesis on calcium isotope variations in Lower-Middle Triassic carbonate rocks. *Chemical Geology*, *471*, 13–37. https://doi.org/10.1016/j.chemgeo.2017.09.006

Lehrmann, D. J., Stepchinski, L., Altiner, D., Orchard, M. J., Montgomery, P., Enos, P., Ellwood, B. B., Bowring, S. A., Ramezani, J., Wang, H., Wei, J., Yu, M., Griffiths, J. D., Minzoni, M., Schaal, E. K., Li, X., Meyer, K. M., & Payne, J. L. (2015). An integrated biostratigraphy (conodonts and foraminifers) and chronostratigraphy (paleomagnetic reversals, magnetic susceptibility, elemental chemistry, carbon isotopes and geochronology) for the Permian–Upper Triassic strata of Guandao section, Nanpanjiang Basin, south China. *Journal of Asian Earth Sciences*, *108*, 117–135. https://doi.org/10.1016/j.jseaes.2015.04.030

Li, F., Penman, D., Planavsky, N., Knudsen, A., Zhao, M., Wang, X., Isson, T. T., Huang, K., Wei, G., Zhang, S., Shen, J., Zhu, X., & Shen, B. (2021). Reverse weathering may amplify post-Snowball atmospheric carbon dioxide levels. *Precambrian Research*, *364*, 106279. https://doi.org/10.1016/j.precamres.2021.106279

Li, G., & West, A. J. (2014). Evolution of Cenozoic seawater lithium isotopes: Coupling of global denudation regime and shifting seawater sinks. *Earth and Planetary Science Letters*, *401*, 284–293. https://doi.org/10.1016/j.epsl.2014.06.011

Li, W., & Liu, X.-M. (2022). Mineralogy and fluid chemistry controls on lithium isotope fractionation during clay adsorption. *Science of The Total Environment*, *851*, 158138. https://doi.org/10.1016/j.scitotenv.2022.158138

Li, X., Hu, Y., Guo, J., Lan, J., Lin, Q., Bao, X., Yuan, S., Wei, M., Li, Z., Man, K., Yin, Z., Han, J., Zhang, J., Zhu, C., Zhao, Z., Liu, Y., Yang, J., & Nie, J. (2022). A high-resolution climate simulation dataset for the past 540 million years. *Scientific Data*, *9*(1), 371. https://doi.org/10.1038/s41597-022-01490-4

Liu, X.-F., Liu, X.-M., Wang, X.-K., Zhai, S., & Liu, X. (2023). Dolostone as a reliable tracer of seawater lithium isotope composition. *Communications Earth & Environment*, *4*(1), 58. https://doi.org/10.1038/s43247-023-00711-x

Lui-Heung, C., & Edmond, J. M. (1988). Variation of lithium isotope composition in the marine environment: A preliminary report. *Geochimica et Cosmochimica Acta*, *52*(6), 1711–1717. https://doi.org/10.1016/0016-7037(88)90239-6

Marcoux, J., & Baud, A. (1986). The Permo-Triassic boundary in the Antalya Nappes (Western Taurides, Turkey). *Memorie Della Società Geologica Italiana*, *34*, 243–252.

Marriott, C. S., Henderson, G. M., Belshaw, N. S., & Tudhope, A. W. (2004). Temperature dependence of δ^7Li, δ^{44}Ca and Li/Ca during growth of calcium carbonate. *Earth and Planetary Science Letters*, *222*(2), 615–624. https://doi.org/10.1016/j.epsl.2004.02.031

Marriott, C. S., Henderson, G. M., Crompton, R., Staubwasser, M., & Shaw, S. (2004). Effect of mineralogy, salinity, and temperature on Li/Ca and Li isotope composition of calcium carbonate. *Chemical Geology*, *212*(1–2), 5–15. https://doi.org/10.1016/j.chemgeo.2004.08.002

Martin, E. E., & Macdougall, J. D. (1995). Sr and Nd isotopes at the Permian/Triassic boundary: A record of climate change. *Chemical Geology*, *125*, 73–99. https://doi.org/10.1016/0009-2541(95)00081-V

Misra, S., & Froelich, P. N. (2012). Lithium Isotope History of Cenozoic Seawater: Changes in Silicate Weathering and Reverse Weathering. *Science*, *335*(6070), 818–823. https://doi.org/10.1126/science.1214697

Monod, O. (1997). *Recherches géologiques dans le Taurus occidental au sud de Beyşehir (Turquie)* [Doctoral dissertation]. Université de Paris-Sud.

Montenegro, A., Spence, P., Meissner, K. J., Eby, M., Melchin, M. J., & Johnston, S. T. (2011). Climate simulations of the Permian-Triassic boundary: Ocean acidification and the extinction event. *Paleoceanography*, *26*(3), PA3207. https://doi.org/10.1029/2010PA002058

Murphy, J. G., Ahm, A.-S. C., Swart, P. K., & Higgins, J. A. (2022). Reconstructing the lithium isotopic composition (δ^7Li) of seawater from shallow marine carbonate sediments. *Geochimica et Cosmochimica Acta*, *337*, 140–154. https://doi.org/10.1016/j.gca.2022.09.019

Musashi, M., Isozaki, Y., Koike, T., & Kreulen, R. (2001). Stable carbon isotope signature in mid-Panthalassa shallow-water carbonates across the Permo–Triassic boundary: Evidence for ^{13}C-depleted superocean. *Earth and Planetary Science Letters*, *191*(1–2), 9–20. https://doi.org/10.1016/S0012-821X(01)00398-3

Nadeau, M. D., Murphy, J. G., Hagen, C. J., Wu, Z., Akhtar, A. A., Ahm, A.-S., Stolper, D. A., Maloof, A. C., & Higgins, J. A. (2025). Disentangling global geochemical signals from local diagenetic alteration in shallow-water marine carbonates during OAE1a. *Earth and Planetary Science Letters*, *666*, 119513. https://doi.org/10.1016/j.epsl.2025.119513

Newell, N. D. (1967). Revolutions in the History of Life. In *Uniformity and Simplicity: A Symposium on the Principle of the Uniformity of Nature* (pp. 63–92). https://doi.org/10.1130/SPE89-p63

Nsingi, J. M., Cui, Y., Cepin, E., Beaty, B., Planavsky, N., Wu, Q., Adloff, M., Wang, J., Selby, D., Liu, Z., Dong, Y., Jiang, S., & Zhu, F. (2025). Changes in continental weathering across the Permian-Triassic transition: A global review. *Global and Planetary Change*, *254*, 105015. https://doi.org/10.1016/j.gloplacha.2025.105015

Özgül, N. (1997). Stratigraphy of the tectono-stratigraphic units in the region Bozkir–Hadim–Taşkent (northern central Taurides). *Bulletin of the Mineral Research and Exploration Institute of Turkey*, *119*, 113–174.

Payne, J. L., & Clapham, M. E. (2012). End-Permian Mass Extinction in the Oceans: An Ancient Analog for the Twenty-First Century? *Annual Review of Earth and Planetary Sciences*, *40*(1), 89–111. https://doi.org/10.1146/annurev-earth-042711-105329

Payne, J. L., Lehrmann, D. J., Follett, D., Seibel, M., Kump, L. R., Riccardi, A., Altiner, D., Sano, H., & Wei, J. (2007). Erosional truncation of uppermost Permian shallow-marine carbonates and implications for Permian-Triassic boundary events. *Geological Society of America Bulletin*, *119*(7–8), 771–784. https://doi.org/10.1130/B26091.1

Payne, J. L., Lehrmann, D. J., Wei, J., Orchard, M. J., Schrag, D. P., & Knoll, A. H. (2004). Large Perturbations of the Carbon Cycle During Recovery from the End-Permian Extinction. *Science*, *305*(5683), 506–509. https://doi.org/10.1126/science.1097023

Payne, J. L., Turchyn, A. V., Paytan, A., DePaolo, D. J., Lehrmann, D. J., Yu, M., & Wei, J. (2010). Calcium isotope constraints on the end-Permian mass extinction. *Proceedings of the National Academy of Sciences*, *107*(19), 8543–8548. https://doi.org/10.1073/pnas.0914065107

Pogge von Strandmann, P. A. E., Burton, K. W., James, R. H., van Calsteren, P., & Gislason, S. R. (2010). Assessing the role of climate on uranium and lithium isotope behaviour in rivers draining a basaltic terrain. *Chemical Geology*, *270*(1–4), 227–239. https://doi.org/10.1016/j.chemgeo.2009.12.002

Pogge von Strandmann, P. A. E., Burton, K. W., James, R. H., van Calsteren, P., Gíslason, S. R., & Mokadem, F. (2006). Riverine behaviour of uranium and lithium isotopes in an actively glaciated basaltic terrain. *Earth and Planetary Science Letters*, *251*(1–2), 134–147. https://doi.org/10.1016/j.epsl.2006.09.001

Pogge von Strandmann, P. A. E., Dellinger, M., & West, A. J. (2021). *Lithium isotopes: A tracer of past and present silicate weathering*. Cambridge University Press. https://doi.org/10.1017/9781108990752

Pogge von Strandmann, P. A. E., Desrochers, A., Murphy, M. J., Finlay, A. J., Selby, D., & Lenton, T. M. (2017). Global climate stabilisation by chemical weathering during the Hirnantian glaciation. *Geochemical Perspectives Letters*, 230–237. https://doi.org/10.7185/geochemlet.1726

Pogge von Strandmann, P. A. E., Fraser, W. T., Hammond, S. J., Tarbuck, G., Wood, I. G., Oelkers, E. H., & Murphy, M. J. (2019). Experimental determination of Li isotope behaviour during basalt weathering. *Chemical Geology*, *517*, 34–43. https://doi.org/10.1016/j.chemgeo.2019.04.020

Pogge von Strandmann, P. A. E., Jenkyns, H. C., & Woodfine, R. G. (2013). Lithium isotope evidence for enhanced weathering during Oceanic Anoxic Event 2. *Nature Geoscience*, *6*(8), 668–672. https://doi.org/10.1038/ngeo1875

Pogge von Strandmann, P. A. E., Jones, M. T., West, A. J., Murphy, M. J., Stokke, E. W., Tarbuck, G., Wilson, D. J., Pearce, C. R., & Schmidt, D. N. (2021). Lithium isotope evidence for enhanced weathering and erosion during the Paleocene-Eocene Thermal Maximum. *Science Advances*, *7*(42), eabh4224. https://doi.org/10.1126/sciadv.abh4224

Pogge von Strandmann, P. A. E., Schmidt, D. N., Planavsky, N. J., Wei, G., Jones, C. L. C., & Baumann, K.-H. (2019). Assessing bulk carbonates as archives for seawater Li isotope ratios. *Chemical Geology*, *530*, 119338. https://doi.org/10.1016/j.chemgeo.2019.119338

R Core Team. (2024). *R: A language and environment for statistical computing*. https://doi.org/10.32614/r.manuals

Rauzi, S., Foster, W. J., Takahashi, S., Hori, R. S., Beaty, B. J., Tarhan, L. G., & Isson, T. T. (2024). Lithium isotopic evidence for enhanced reverse weathering during the Early Triassic warm period. *Proceedings of the National Academy of Sciences*, *121*(32), e2318860121. https://doi.org/10.1073/pnas.2318860121

Retallack, G. J. (1995). Permian-Triassic Life Crisis on Land. *Science*, *267*(5194), 77–80. https://doi.org/10.1126/science.267.5194.77

Retallack, G. J. (1999). Postapocalyptic greenhouse paleoclimate revealed by earliest Triassic paleosols in the Sydney Basin, Australia. *Geological Society of America Bulletin*, *111*(1), 52–70. https://doi.org/10.1130/0016-7606(1999)111%3C0052:PGPRBE%3E2.3.CO;2

Romano, C., Goudemand, N., Vennemann, T. W., Ware, D., Schneebeli-Hermann, E., Hochuli, P. A., Brühwiler, T., Brinkmann, W., & Bucher, H. (2013). Climatic and biotic upheavals following the end-Permian mass extinction. *Nature Geoscience*, *6*(1), 57–60. https://doi.org/10.1038/ngeo1667

Rugenstein, J. K. C., Ibarra, D. E., & von Blanckenburg, F. (2019). Neogene cooling driven by land surface reactivity rather than increased weathering fluxes. *Nature*, *571*(7763), 99–102. https://doi.org/10.1038/s41586-019-1332-y

Sano, H., & Nakashima, K. (1997). Lowermost Triassic (Griesbachian) microbial bindstone-cementstone facies, southwest Japan. *Facies*, *36*(1), 1–24. https://doi.org/10.1007/BF02536874

Sauzéat, L., Rudnick, R. L., Chauvel, C., Garçon, M., & Tang, M. (2015). New perspectives on the Li isotopic composition of the upper continental crust and its weathering signature. *Earth and Planetary Science Letters*, *428*, 181–192. https://doi.org/10.1016/j.epsl.2015.07.032

Scotese, C. R. (2014). *Atlas of Phanerozoic rainfall maps (Mollweide projection): Volumes 1-6, PALEOMAP atlas for ArcGIS*. PALEOMAP Project.

Sedlacek, A. R. C., Saltzman, M. R., Algeo, T. J., Horacek, M., Brandner, R., Foland, K., & Denniston, R. F. (2014). $^{87}Sr/^{86}Sr$ stratigraphy from the Early Triassic of Zal, Iran: Linking temperature to weathering rates and the tempo of ecosystem recovery. *Geology*, *42*(9), 779–782. https://doi.org/10.1130/G35545.1

Seyedali, M., Coogan, L. A., & Gillis, K. M. (2021). The effect of solution chemistry on elemental and isotopic fractionation of lithium during inorganic precipitation of calcite. *Geochimica et Cosmochimica Acta*, *311*, 102–118. https://doi.org/10.1016/j.gca.2021.07.021

Silva-Tamayo, J. C., Lau, K. V., Jost, A. B., Payne, J. L., Wignall, P. B., Newton, R. J., Eisenhauer, A., Depaolo, D. J., Brown, S., Maher, K., Lehrmann, D. J., Altiner, D., Yu, M., Richoz, S., & Paytan, A. (2018). Global perturbation of the marine calcium cycle during the Permian-Triassic transition. *Geological Society of America Bulletin*, *130*(7–8), 1323–1338. https://doi.org/10.1130/B31818.1

Song, H., Tong, J., Algeo, T. J., Song, H., Qiu, H., Zhu, Y., Tian, L., Bates, S., Lyons, T. W., Luo, G., & Kump, L. R. (2014). Early Triassic seawater sulfate drawdown. *Geochimica et Cosmochimica Acta*, *128*, 95–113. https://doi.org/10.1016/j.gca.2013.12.009

Song, H., Wignall, P. B., Tong, J., Song, H., Chen, J., Chu, D., Tian, L., Luo, M., Zong, K., Chen, Y., Lai, X., Zhang, K., & Wang, H. (2015). Integrated Sr isotope variations and global environmental changes through the Late Permian to early Late Triassic. *Earth and Planetary Science Letters*, *424*, 140–147. https://doi.org/10.1016/j.epsl.2015.05.035

Sun, H., Xiao, Y., Gao, Y., Zhang, G., Casey, J. F., & Shen, Y. (2018). Rapid enhancement of chemical weathering recorded by extremely light seawater lithium isotopes at the Permian–Triassic boundary. *Proceedings of the National Academy of Sciences*, *115*(15), 3782–3787. https://doi.org/10.1073/pnas.1711862115

Sun, Y., Joachimski, M. M., Wignall, P. B., Yan, C., Chen, Y., Jiang, H., Wang, L., & Lai, X. (2012). Lethally Hot Temperatures During the Early Triassic Greenhouse. *Science*, *338*(6105), 366–370. https://doi.org/10.1126/science.1224126

Taylor, H. L., Duivestein, I. J. K., Farkas, J., Dietzel, M., & Dosseto, A. (2019). Technical note: Lithium isotopes in dolostone as a palaeo-environmental proxy – an experimental approach. *Climate of the Past*, *15*(2), 635–646. https://doi.org/10.5194/cp-15-635-2019

Teng, F.-Z., McDonough, W. F., Rudnick, R. L., Dalpé, C., Tomascak, P. B., Chappell, B. W., & Gao, S. (2004). Lithium isotopic composition and concentration of the upper continental crust. *Geochimica et Cosmochimica Acta*, *68*(20), 4167–4178. https://doi.org/10.1016/j.gca.2004.03.031

Tomascak, P. B., Magna, T., & Dohmen, R. (2016). *Advances in Lithium Isotope Geochemistry*. Springer International Publishing. https://doi.org/10.1007/978-3-319-01430-2

Ünal, E., Altiner, D., Yilmaz, I. O., & Ozkan-Altiner, S. (2003). Cyclic sedimentation across the Permian-Triassic boundary (central Taurides, Turkey). *Rivista Italiana Di Paleontologia e Stratigrafia*, *109*(2), 359–376. https://doi.org/10.13130/2039-4942/5511

Vigier, N., Decarreau, A., Millot, R., Carignan, J., Petit, S., & France-Lanord, C. (2008). Quantifying Li isotope fractionation during smectite formation and implications for the Li cycle. *Geochimica et Cosmochimica Acta*, *72*(3), 780–792. https://doi.org/10.1016/j.gca.2007.11.011

Vigier, N., Gislason, S. R., Burton, K. W., Millot, R., & Mokadem, F. (2009). The relationship between riverine lithium isotope composition and silicate weathering rates in Iceland. *Earth and Planetary Science Letters*, *287*(3–4), 434–441. https://doi.org/10.1016/j.epsl.2009.08.026

Vigier, N., Rollion-Bard, C., Spezzaferri, S., & Brunet, F. (2007). In situ measurements of Li isotopes in foraminifera. *Geochemistry, Geophysics, Geosystems*, *8*(1), 2006GC001432. https://doi.org/10.1029/2006GC001432

Wang, J., Jacobson, A. D., Zhang, H., Ramezani, J., Sageman, B. B., Hurtgen, M. T., Bowring, S. A., & Shen, S.-Z. (2019). Coupled $\delta^{44/40}$Ca, $\delta^{88/86}$Sr, and ^{87}Sr/^{86}Sr geochemistry across the end-Permian mass extinction event. *Geochimica et Cosmochimica Acta*, *262*, 143–165. https://doi.org/10.1016/j.gca.2019.07.035

Wang, W.-Q., Zhang, F., Liu, C.-Y., Pogge von Strandmann, P. A. E., Xiong, G., Zheng, Q., Garbelli, C., Zhang, Y., Yuan, D., & Shen, S.-Z. (2024). Constraints on the continental weathering intensity through the Permian using lithium isotopes of well-preserved brachiopod shells. *Earth and Planetary Science Letters*, *648*, 119101. https://doi.org/10.1016/j.epsl.2024.119101

Wei, G.-Y., Zhang, F., Yin, Y.-S., Lin, Y.-B., Pogge von Strandmann, P. A. E., Cao, M., Li, N., Xiong, G., Chen, X., Fan, C., Xu, C., Tan, F., Zhang, X., Yang, H., Ling, H.-F., & Shen, S.-Z. (2023). A 13 million-year record of Li isotope compositions in island carbonates: Constraints on bulk inorganic carbonate as a global seawater Li isotope archive. *Geochimica et Cosmochimica Acta*, *344*, 59–72. https://doi.org/10.1016/j.gca.2023.01.013

Weldeghebriel, M. F., & Lowenstein, T. K. (2023). Seafloor hydrothermal systems control long-term changes in seawater [Li^+]: Evidence from fluid inclusions. *Science Advances*, *9*(30), eadf1605. https://doi.org/10.1126/sciadv.adf1605

Yang, C., Vigier, N., Lian, E., Lai, Z., & Yang, S. (2021). Decoupling of dissolved and particulate Li isotopes during estuarine processes. *Geochemical Perspectives Letters*, 40–44. https://doi.org/10.7185/geochemlet.2133

Yang, F., Sun, Y. D., Frings, P. J., Luo, L., E, J. W., Wang, L. N., Huang, Y. F., Wang, T., Müller, J., & Xie, S. C. (2022). Collapse of Late Permian chert factories in the equatorial Tethys and the nature of the Early Triassic chert gap. *Earth and Planetary Science Letters*, *600*, 117861. https://doi.org/10.1016/j.epsl.2022.117861

Yin, Y.-S., Wei, G.-Y., Pogge von Strandmann, P. A. E., Lechte, M. A., Hohl, S. V., Lin, Y.-B., Li, D., Chen, T., Yang, T., Zhang, F., Isson, T. T., Zhang, H., Cai, Y., & Ling, H.-F. (2023). Widespread clay authigenesis and highly congruent silicate weathering in the Marinoan aftermath. *Earth and Planetary Science Letters*, *623*, 118423. https://doi.org/10.1016/j.epsl.2023.118423

Zeebe, R. E., & Wolf-Gladrow, D. A. (2009). Carbon Dioxide, Dissolved (Ocean). In V. Gornitz (Ed.), *Encyclopedia of Paleoclimatology and Ancient Environments* (pp. 123–127). Springer. https://doi.org/10.1007/978-1-4020-4411-3_30

Zhang, F., Algeo, T. J., Romaniello, S. J., Cui, Y., Zhao, L., Chen, Z.-Q., & Anbar, A. D. (2018). Congruent Permian-Triassic δ^{238}U records at Panthalassic and Tethyan sites: Confirmation of global-oceanic anoxia and validation of the U-isotope paleoredox proxy. *Geology*, *46*(4), 327–330. https://doi.org/10.1130/G39695.1

Zhang, F., Dellinger, M., Hilton, R. G., Yu, J., Allen, M. B., Densmore, A. L., Sun, H., & Jin, Z. (2022). Hydrological control of river and seawater lithium isotopes. *Nature Communications*, *13*(1), 3359. https://doi.org/10.1038/s41467-022-31076-y

Zhang, F., Romaniello, S. J., Algeo, T. J., Lau, K. V., Clapham, M. E., Richoz, S., Herrmann, A. D., Smith, H., Horacek, M., & Anbar, A. D. (2018). Multiple episodes of extensive marine anoxia linked to global warming and continental weathering following the latest Permian mass extinction. *Science Advances*, *4*(4), e1602921. https://doi.org/10.1126/sciadv.1602921

Zhang, L., Orchard, M. J., Algeo, T. J., Chen, Z.-Q., Lyu, Z., Zhao, L., Kaiho, K., Ma, B., & Liu, S. (2019). An intercalibrated Triassic conodont succession and carbonate carbon isotope profile, Kamura, Japan. *Palaeogeography, Palaeoclimatology, Palaeoecology*, *519*, 65–83. https://doi.org/10.1016/j.palaeo.2017.09.001

SUPPLEMENTARY MATERIALS

Supplement

Download: https://ajsonline.org/article/156171-heterogeneous-carbonate-lithium-isotope-records-across-the-end-permian-mass-extinction-indicate-a-highly-perturbed-lithium-cycle-in-the-early-triassic/attachment/333327.docx

Table S1

Download: https://ajsonline.org/article/156171-heterogeneous-carbonate-lithium-isotope-records-across-the-end-permian-mass-extinction-indicate-a-highly-perturbed-lithium-cycle-in-the-early-triassic/attachment/333328.docx